FRIS revisited in 2018: On the circulation and water masses at the Filchner and Ronne Ice Shelves in the southern Weddell Sea

[1]Markus A. Janout, [1]Hartmut H. Hellmer, [2]Tore Hattermann, [3]Oliver Huhn, [3]Jürgen Sültenfuss, [4,5]Svein Østerhus, [1]Lukrecia Stulic, [6]Svenja Ryan, [1]Michael Schröder, [1]Torsten Kanzow

[1]Alfred-Wegener-Institute Helmholtz Center for Polar and Marine Research, Bremerhaven, Germany

[2]Norwegian Polar Institute, Tromsø, Norway

[3]Institute of Environmental Physics, University Bremen, Germany

[4]Norwegian Research Center, Bergen, Norway

[5]Bjerknes Centre for Climate Research, University of Bergen, Norway

[6]Woods Hole Oceanographic Institution, Woods Hole, USA

Corresponding author: Markus Janout (markus.janout@awi.de)

Key Points:

- Hydrographic status update with the first comprehensive CTD survey along the entire FRIS front since 1995
- Strong and stable presence of High Salinity Shelf Water in Ronne Depression over decades
- Dominance of Ronne-sourced Ice Shelf Water in Filchner Trough in 2018 points to intensified sub-FRIS circulation

Abstract

The Filchner-Ronne Ice Shelf (FRIS) is characterized by moderate basal melt rates due to the near-freezing waters that dominate the wide southern Weddell Sea continental shelf. We revisited the region in austral summer 2018 with detailed hydrographic and noble gas surveys along FRIS. The FRIS front was characterized by High Salinity Shelf Water (HSSW) in Ronne Depression, Ice Shelf Water (ISW) on its eastern flank and an inflow of modified Warm Deep Water (mWDW) entering through Central Trough. Filchner Trough was dominated by Ronne HSSW-sourced ISW, likely forced by a recently intensified circulation beneath FRIS due to enhanced sea ice production in the Ronne polynya since 2015. Glacial meltwater fractions and tracer-based water mass dating indicate two separate ISW outflow cores, one hugging the Berkner slope after a two-year travel time, and the other located in the central Filchner Trough following a ~six year-long transit through the FRIS cavity. Historical measurements indicate the presence of two distinct modes, in which water masses in Filchner Trough were dominated by either Ronne HSSW-derived ISW (Ronne-mode) or more locally-derived Berkner-HSSW (Berkner-mode). While the dominance of these modes has alternated on interannual time scales, ocean densities in Filchner Trough have remained remarkably stable since the first surveys in 1980. Indeed, geostrophic velocities indicated outflowing ISW-cores along the trough's western flank and onto Berkner Bank, which suggests that Ronne-ISW preconditions Berkner-HSSW production. The negligible density difference between Berkner- and Ronne-mode waters indicates that each contribute cold dense shelf waters to protect FRIS against inflowing mWDW.

Plain Language Summary

We visited the largest floating Antarctic ice shelf in the southern Weddell Sea in 2018 with an icebreaker expedition, and measured ocean temperature, salinity, meltwater content and other parameters in front of the Filchner-Ronne Ice Shelf. We found that the ocean conditions were still dominated by the very cold and dense waters needed to protect the ice shelf from inflowing warm waters from the deep ocean. We compared the 2018 conditions with earlier surveys since the 1980s and concluded that, in spite of climate change and in contrast to other Antarctic regions, the water masses on the southern Weddell Sea shelf remained relatively stable overall. We found that most of the stations we visited near the Filchner Ice Shelf edge were dominated by cold Ice Shelf Water, which forms when water masses interact with the underside of the shelf ice. Our measurements helped improve our understanding regarding the currents and water masses on the southern Weddell Sea continental shelf.

1) Introduction

The Antarctic continent stores the largest amount of freshwater on earth. However, the Antarctic ice sheets and glaciers are losing mass, leading to a cumulative sea level rise of 14 mm since 1979 (Rignot et al., 2019). Some ice mass loss could be linked to changes in the atmosphere, such as the warming of the Antarctic Peninsula (Vaughan et al., 2003), which triggered the decay of the Larsen ice shelves (Rott et al., 1996; Broeke v.d., 2005). However, the majority of ice mass was lost from glaciers and ice sheets that were exposed to the influence of warm ocean waters (Rignot et al., 2019). Thompson et al. (2018) classify the Antarctic marginal seas into "warm", "fresh", and "dense" shelves based on their hydrographic properties impacted by the dynamics of the Antarctic Slope Current system and associated frontal dynamics. On "warm" continental shelves such as along the West Antarctic Peninsula or in the Amundsen and Bellingshausen Seas, warm waters of open ocean origin intrude inshore by following the seafloor since there is no strong front separating the shelf from the warm Circumpolar Deep Water (CDW) as is found on the "fresh" shelves surrounding the Antarctic continent. The "dense" continental shelves of the Ross and Weddell Seas are wide and dominated by near-freezing conditions (Nicholls et al., 2009) and characterized by moderate ice shelf basal melt rates (Paolo et al., 2015; Rignot et al., 2019). The Filchner-Ronne Ice Shelf (FRIS), Antarctica's largest ice shelf by volume, is located south of such a "dense" wide continental shelf in the Weddell Sea. The circulation and oceanographic conditions on this southern Weddell Sea shelf are dominated by a saline water mass named High Salinity Shelf Water (HSSW). HSSW is at surface-freezing temperature (~ -1.9 °C) and forms as a result of sea ice production on the continental shelf and in coastal polynyas, in particular in the southwestern Weddell Sea off Ronne Ice Shelf (RIS, Haid and Timmermann, 2013). HSSW has salinities of 34.60-34.85 and contributes to the dense shelf waters or directly flows off the shelf across the continental slope and contributes to the formation of Weddell Sea Deep and Bottom Waters (Gordon et al., 1993; Orsi et al., 1999), which are precursors of Antarctic Bottom Water (AABW). Data from moorings at the ice shelf front (Nicholls et al., 2004), sub-ice shelf moorings (Nicholls et al., 2001), and model studies (Timmermann et al., 2012) indicate that HSSW enters the cavity below FRIS following the bathymetry in Ronne Depression and drives an ice shelf-wide thermohaline circulation (Figure 1). En route through the cavity, HSSW may encounter greater water pressures that lower the in situ freezing point to match its own surface-freezing temperature, thereby causing melting at the

base of the ice shelf (model-derived average of 0.34 m year^{-1} at FRIS; Timmermann et al., 2012). The resulting modified water mass is colder and fresher and hence more buoyant and is referred to as Ice Shelf Water (ISW). ISW is characterized by below-surface freezing temperatures (< -1.9°C), and leaves the FRIS cavity via the Filchner Trough (Nicholls et al. 2009).

These cold and dense waters prevent a large-scale inflow of Warm Deep Water (WDW), the Weddell Sea's derivative of CDW, which occupies the intermediate layer (200-1200 m) of the Weddell Sea (Daae et al., 2020). This is not the case along the narrow continental shelf off Dronning Maud Land, where WDW mixes with the colder and fresher Eastern Shelf Water to result in modified (m)WDW, which seasonally penetrates the southern Weddell Sea through troughs intersecting the continental shelf (Ryan et al., 2017). The seasonal flow of mWDW onto the shallower shelf is regulated by the Antarctic Slope Front, which responds to changes in the wind field and stratification (Hattermann, 2018) and controls cross-frontal exchange through mesoscale eddies and instabilities (Nøst et al., 2011; Stewart and Thompson, 2015; Stewart et al., 2018). On FRIS, however, the impact of mWDW is presently limited by the cold, dense waters that occupy the Filchner Trough, though model studies suggest that a freshening of the shelf water masses under warmer atmospheric conditions may lead to enhanced warm water inflow and dramatic ice shelf melting by the end of this century (Hellmer et al., 2012; Hellmer et al., 2017; Daae et al., 2020). MWDW is a persistently observed water mass at the RIS front, west of Berkner Bank (Foldvik et al., 2001; Gammelsrød et al., 1994), and also has been observed at the FIS front (Darelius et al. 2016). Recent moored temperature records indicate considerable interannual variability of mWDW-presence in Filchner Trough (Ryan et al., 2020). At present, this does not appear to significantly contribute to FRIS mass loss, as mWDW resides above the depth of the ice shelf front atop denser waters that occupy the Filchner Trough. However, future melt rates will crucially depend on the evolution of the dense water masses and circulation on the southern Weddell Sea continental shelf.

Prior to 2017, the hydrography at Filchner Ice Shelf (FIS) front was dominated by water masses that were formed on Berkner Bank (Figure 1), referred to as Berkner-HSSW (Akhoudas et al. 2020), and seasonal outflows of ISW along the western flank of the trough (Darelius and Sallée, 2018). However, temperature and salinity records from moorings underneath FRIS have shown an intensification of the Ronne-HSSW driven cavity circulation in response to increased sea ice formation in the Ronne Polynya since 2015. This resulted in a decline in Berkner-HSSW

and an increase in Ronne HSSW-derived ISW in the Filchner Trough in mid-2017 (Hattermann et al., 2021, from here on referred to as H2021). Shortly thereafter, in austral summer 2018, an *RV Polarstern*-expedition (PS111) was able to access both FIS and RIS fronts during extended polynya events and undertake a detailed hydrographic survey.

In this paper, we present a 2018 hydrographic status update of the FRIS front and Filchner Trough, and contrast our findings with those from earlier expeditions. Further, we investigate the variability of circulation regimes underneath FRIS as inferred from observed ocean conditions in Filchner Trough. Specifically, we discuss two contrasting circulation modes that are immediately connected to HSSW production north of RIS and on Berkner Bank, referred to as Ronne- and Berkner-modes. We examine these modes in a historical context and finally discuss the impact of changes in forcing parameters on the regional and large-scale ocean circulation.

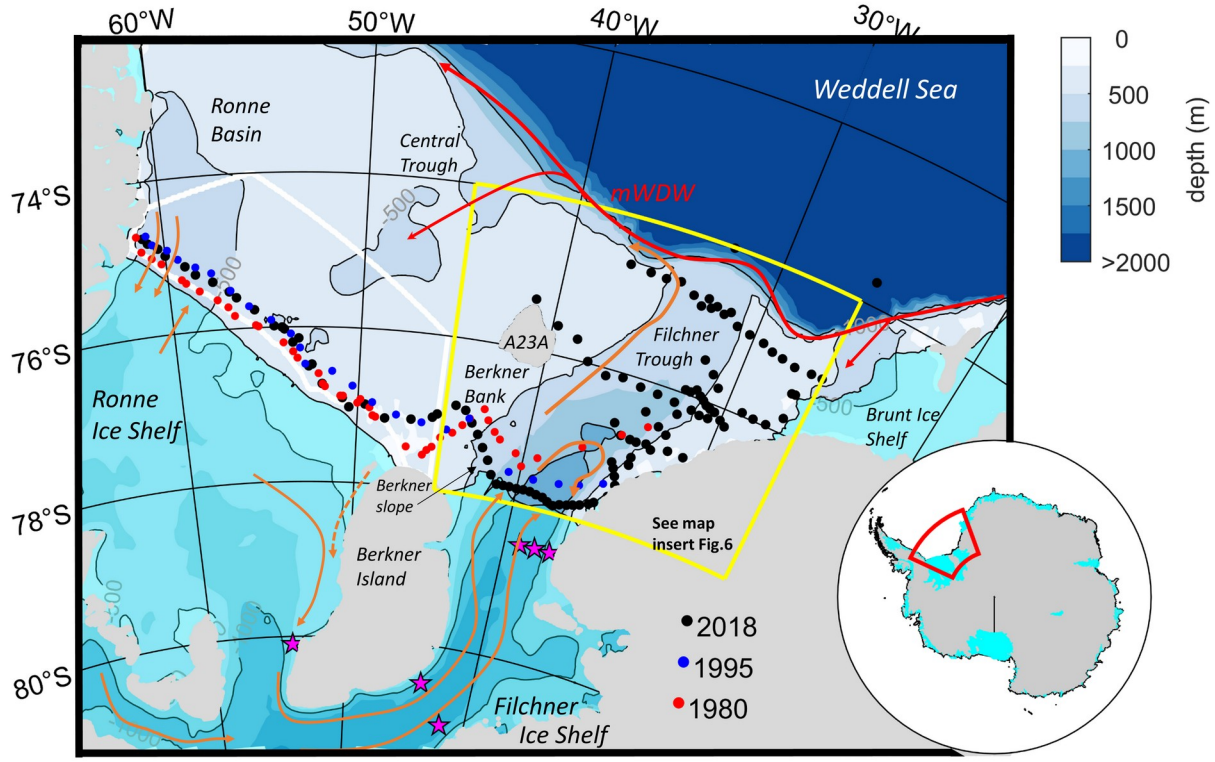

Figure 1: Map of the southern Weddell Sea including CTD stations from 2018 (black), 1995 (blue) and 1980 (red). Magenta stars indicate drillhole moorings mentioned in the text for reference (H2021). Ice Shelves are marked with cyan shading, bathymetry (Schaffer et al., 2016) is shown in blue color contours. The 500 m and 1000 m-isobaths are marked with black contours. Bathymetric and geographic features referred to in the text are indicated in the map. The area north of RIS inside the white line marks the region used to quantify sea ice production (Figure 12). The Filchner Trough framed by the yellow lines marks the inset used in Figure 6. The

arrows indicate the inflow branches of modified Warm Deep Water (red) and the under-FRIS circulation fueled by the inflow of High Salinity Shelf Water (orange).

2) Materials and Methods

2.1 Hydrographic data

Hydrographic measurements were carried out onboard the German research icebreaker *RV Polarstern* (Alfred-Wegener-Institut Helmholtz-Zentrum für Polar- und Meeresforschung, 2017) during the PS111-expedition to the southern Weddell Sea (Figure 1) from 12 January to 14 March 2018 from Cape Town, South Africa, to Punta Arenas, Chile. Temperature and salinity profiles during PS111 (Janout et al., 2019) were collected with a Seabird 911+ CTD (Conductivity-Temperature-Depth) recorder attached to a water sampling carousel. The raw data were processed with the Seabird processing software and quality controlled thereafter. Pre- and post-cruise calibrations of the conductivity and temperature sensors were performed by the manufacturer. Finally, the salinity values were corrected with salinity measurements from water samples, which were measured with an Optimare Precision Salinometer. The final accuracies of the CTD data are estimated as 0.0005°C and 0.002 for temperature and salinity, respectively. Dissolved oxygen measurements were collected with an oxygen sensor attached to the CTD. The sensor was carefully calibrated throughout the expedition by measuring the oxygen content of water samples using the Winkler titration method. Along-track oceanographic and meteorological parameters were measured with *RV Polarstern*'s fixed installed underway measurement system. Temperature and conductivity at 11 m (Figure 2a-b) were measured with a thermosalinograph SBE21 (Schröder and Rohardt, 2018) with accuracies of 0.001°C and 0.001 S/m. Air temperature, wind speed and direction, and atmospheric pressure (Figure 2c-f) were measured with Polarstern's weather system (Schmitthüsen, 2020).

Geostrophic velocities were computed from the density structure measured via CTD stations along FRIS assuming a level-of-no-motion at 200 m as this is the minimum thickness of the edge along FRIS (Schaffer et al., 2016). In order to distinguish between ISW sourced from either Ronne- or Berkner-HSSW, we defined the respective source water salinities by finding the crossing point of the ISW Gade line (Gade, 1979) with the surface freezing temperature line. This method assumes water mass transformation along characteristic lines in temperature-

salinity-space in the absence of other mixing end members. We neglected the effect of heat conduction at the ice shelf-ocean interface and used a slope of 2.4 K/psu of the Gade line, resulting from $\Delta T/\Delta S=L/(S_0 c_p)$, where the latent heat of ice is $L=3.34 \times 10^5$ J kg^{-1} , the specific heat capacity of seawater cp= 4186 J kg^{-1} K^{-1}, and S_0 is the seawater salinity.

We revisited earlier hydrographic stations to view the 2018-observations in a decadal context and to understand the variability in hydrographic properties and tracers along the FRIS front. Prior to 2018, the most comprehensive surveys along FRIS took place in 1980 (early January to mid-February) aboard the *RV Polarsirkel* (Gammelsrød and Slotsvik, 1981) and in 1995 (late January to early March) aboard *RV Polarstern* (Schröder, 2010). We use CTD stations from both earlier surveys and in addition tracer data from 1995. Similar to PS111, both historic surveys entered the Ronne ice front region through polynyas, and CTD stations were approximately sampled at the same relative distance from the shelf ice. For an interannual comparison of source water salinities in Filchner Trough, we further investigated historical CTD stations collected between 1973 and 2018 (see Carmack and Foster, 1975; Foldvik et al., 1985; Driemel et al., 2017 for historic data details).

2.2 Glacial basal melt water (GBMW) from oceanic noble gas measurements

Water samples from the CTD-rosette-system were collected in gas tight copper tubes and subsequently analyzed for noble gas content with the IUP Bremen mass spectrometer (Sültenfuß et al, 2009). Oceanic measurements of the low-solubility and stable noble gases helium (He) and neon (Ne) provide a useful tool to identify and quantify GBMW (e.g. Schlosser et al. 1986; Hohmann et al., 2002; Huhn et al., 2008; Huhn et al., 2018; Rhein et al, 2018). Atmospheric air with a constant composition of these noble gases is trapped in the ice matrix during formation of the meteoric ice. Due to the enhanced hydrostatic pressure at the ice shelf base, these gases are completely dissolved in the water when the ice melts. This leads to a He concentration of 25.7 nmol/kg and a Ne concentration of 90.1 nmol/kg in pure GBMW (Loose and Jenkins, 2014). GBMW is detectable at fractions of <0.05% based on an accuracy of <0.5% for He measurements performed at the IUP Bremen. Some GBMW may be enriched with crustal He (i.e., the isotope ^{4}He) from α-decay of uranium, thorium, and their daughter products in the bedrock beneath an ice sheet. On geological timescales, the crustal He accumulates in the overlying ice up to 300 m above the bedrock (Beaird et al., 2015; Suess and Wänke, 1963). A He

surplus of 4.5 ± 0.5 times that of GBMW has been observed in deep ice near to bedrock. Some He (mainly primordial ^{3}He) is released by mid-ocean ridges to the ocean's interior by hydrothermal activity (Clarke et al., 1969; Well et al., 2003), increasing the ^{3}He/^{4}He ratio (expressed as δ^3He in %) in the water versus the equilibrium ratio. We used the He and Ne concentrations and the method from Rhein et al. (2018) to calculate the fractions of GBMW. First, we estimated the mean mixed layer supersaturation from noble gas stations at a distance from the ice shelf front (to avoid bias from upwelled GBMW into the mixed layer) and subtracted this value from the measured values. Then, we subtracted the equilibrium value $He_{EQ}(\theta,S)$ and $Ne_{EQ}(\theta,S)$ (for each data point as a function of the local potential temperature θ and salinity S using the solubility function from Weiss (1971)) from the observed values and attributed the remainder to pure GBMW. In this paper, we show GBMW calculated from Ne to exclude any bias from additional crustal He.

Additionally, we analyzed 335 seawater samples for the transient tracers chlorofluorocarbon CFC-12 and sulphur hexafluoride SF_6. These anthropogenic trace gases have increased in the atmosphere due to rising human production and enter the ocean via gas exchange at the ocean surface. Hence, they allow us to determine transit time scales of oceanic transport (Smethie et al., 2001; Waugh et al., 2003; Huhn et al., 2013). Samples were filled from the CTD-rosette-system into glass ampoules avoiding atmospheric contact. The ampules were flame-sealed after a tracer-free headspace of purified nitrogen was applied. Later, at IUP Bremen, the samples were analyzed by purge and trap pre-treatment followed by gas chromatographic (GC) separation on a capillary column and electron capture detection (ECD) (Bulsiewicz et al., 1998). The total error of the measurement was ± 2 % for CFC-12 and ± 5 % for SF_6. Here, we show the partial pressure of these trace gases in the samples instead of concentration to account for the solubility of these gases under different temperatures and salinities (Warner and Weiss, 1985; Bullister et al., 2002).

Water mass ages (i.e. the time lag between the last contact with the atmosphere and time of observation) were determined from the ratio of SF_6/CFC-12. The ratio excludes the effect of mixing with old (tracer-free) water and possible saturation dis-equilibria during formation (assuming identical equilibration fractions for both tracers). First, we calculated the partial pressure of these gases in each sample from the concentrations, temperature and salinity using the solubility functions from Warner and Weiss (1985) and Bullister et al. (2002). Second, we

compared the partial pressure ratio in each sample with the known atmospheric ratio time history (Bullister, 2017), and determined the year of equilibration with the atmosphere and finally the age as the time lag between year of observation and formation.

2.3 Ronne sea ice production estimates

The highest sea ice production rates in the southern Weddell Sea are found in coastal polynyas, areas characterized by open water, thin ice, and low sea ice concentration (Paul et al., 2015). Coastal polynyas form all along FRIS, driven by offshore winds and tides. We used results from a simulation with the global Finite Element Sea ice–ice shelf–Ocean Model (FESOM, Timmermann et al. (2012), Wang et al., 2014) to derive sea ice production estimates in polynyas associated to the Ronne sector (white framed area in Figure 1) in the southern Weddell Sea (1985-2017). The model was run on a grid with horizontal resolution that varied between 3 km under the ice shelves, 6-7 km along Ronne Ice Front, and up to 25 km north of the Weddell Sea continental shelf. We used a hybrid vertical coordinate system with 36 layers. Ice shelf draft, cavity geometry, and global ocean bathymetry were prepared from the 1-minute version of RTopo-2 (Schaffer et al., 2016). This model was initialized in 1979 from temperature and salinity derived from the World Ocean Atlas 2009 (Levitus et al., 2010), and run until the end of 2017 using atmospheric forcing from the ERA-Interim reanalysis (Dee et al., 2011) on a 75 km horizontal grid, with 6-hourly air and dew point temperatures (both at 2 m altitude), 10 m-wind fields, as well as 12-hourly average shortwave and longwave radiation, precipitation and evaporation values. We calculated cumulative annual ice production within polynyas in the Ronne sector (Figure 1) from the daily data. Only positive sea ice production rates were taken into account, and nodes with sea ice concentration <70% or thickness <20 cm were considered to be polynyas.

3) Results

3.1 Surface hydrography on the southern Weddell Sea shelf in February 2018

In February 2018 the near-surface (11 m) southern Weddell Sea shelf water was characterized by predominantly cold and saline conditions, with average along-track temperature and salinity of -1.6°C and 33.9, respectively (Figure 2). During the sampling period, heavy sea

ice conditions in the southern Weddell Sea inhibited access to the slope region west of ~36°W. However, extensive open water regions were found in a large polynya along the eastern Filchner Trough and near the shelf break in the northeast, where maximum temperatures of -0.8°C were measured in early February. The warm temperatures then vanished during the second visit to the region in late February, with the sea ice cover rapidly closing under freezing air temperatures (Figure 2c) during the transition to winter conditions. Southwest of the grounded iceberg *A23A* (Figure 2), an extended region with decreased sea ice concentration, which had been apparent since November 2017 (not shown), developed into open water by February 2018. This region (45-50°W) is within the mWDW-inflow region along Central Trough that will be discussed in more detail later, and showed above-freezing surface waters of -1.3°C during our transit on 10 February 2018 (Figure 2a). Tides are considerable on the southwest Weddell Sea shelf (Makinson, 2002) and likely cause upward heat fluxes of the mWDW to the surface, which may contribute to the local reduction in sea ice concentration there. All other regions along the cruise-track featured near-freezing surface waters. In particular, the westernmost track along RIS was carried out along a narrow (~5-10 km) polynya caused by southerly winds before and during our visit in early-to-mid February 2018 (Figure 2d-e), which led to active sea ice formation with minimum air temperatures reaching below -20°C (Figure 2c) during the time of our observations. Surface salinities showed considerable gradients from the northeast to the southwest (Figure 2b). The northeast is influenced by local and advected meltwater with minimum salinities of 33.5 and slightly higher values of up to 34.0 toward the FIS edge. Maximum surface salinites of 34.5 were found in front of RIS.

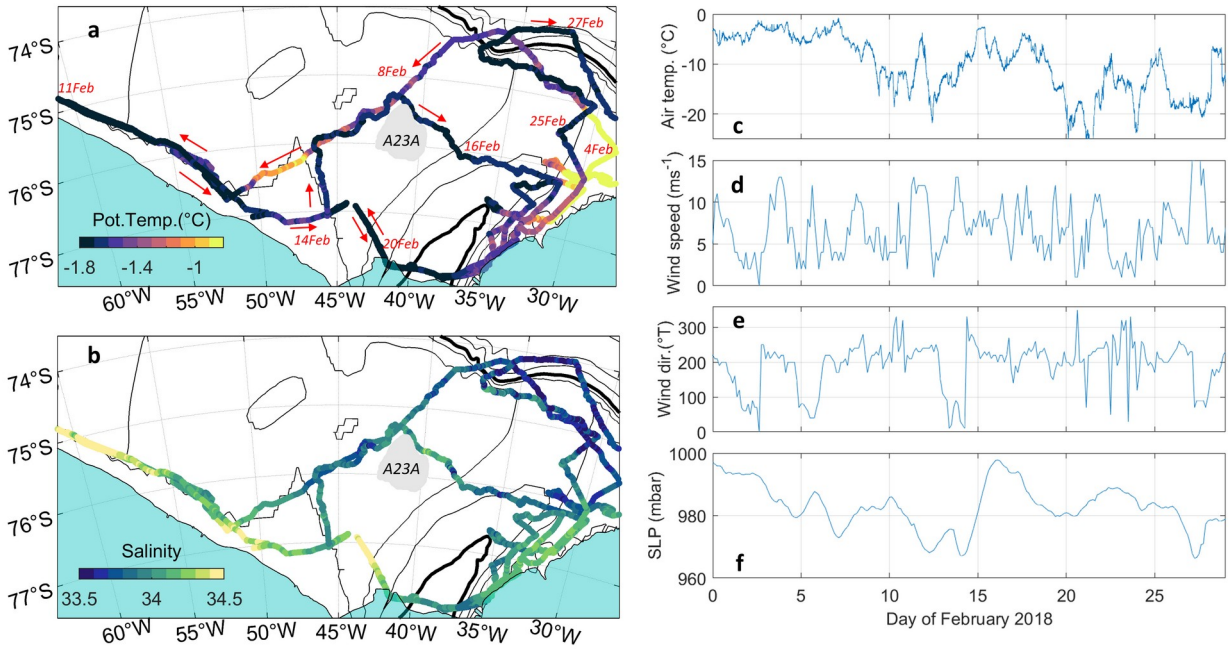

Figure 2: Along-track a) temperature (°C) and b) salinity measured by the ship's thermosalinograph at 11 m water depth, c) air temperature (°C), d) wind speed (m s^{-1}) and e) direction (°T); f) sea level pressure (mbar) measured locally by RV Polarstern's weather system displayed against the day of February. Arrows indicating travel direction and occupation dates in panel a) are provided for better orientation. Cyan shading in a) and b) indicate ice sheets and ice shelves. Bathymetry contours in black mark every 500 m; the 1000 m-isobath is marked by the bold line.

3.2 Hydrographic conditions along the Filchner-Ronne Ice Shelf edge and in Filchner Trough in 2018

The hydrography along the RIS front in austral summer 2018 was dominated by HSSW with salinities of up to 34.84 in the deepest part of Ronne Depression (Figure 3a-b). The overlying water column was salinity-stratified with temperatures near the freezing point from surface to bottom. Thermohaline measurements indicated the presence of an ISW core located on the eastern flank of Ronne Depression carrying temperatures of -2.1°C. Furthermore, the ISW sampled was found to possess high levels of ΔHe and ΔNe (not shown) and was thus enriched in GBMW (0.8 %, Figure 4a). Geostrophic velocities suggested a 1-5 cm s^{-1} northward flow (Figure 5). Another previously identified outflow branch (Nicholls et al., 2004) appeared on the western edge of this transect at 60°W, although without super-cooled waters and only slightly enriched in GBMW (0.5%, Figure 4a). The hydrography further east near Berkner Bank around 52°W was characterized by the inflow of -1.5°C-mWDW that was guided from the shelf break toward the

ice shelf front along Central Trough (Figure 1). The mWDW present at the continental slope was significantly warmer than the -1.5°C-waters observed at the ice shelf edge (i.e. the maximum temperature in transect number 4 in Figure 6 was -0.2 °C), which suggests that a substantial amount of mWDW-heat was lost during the ~500 km-long route across the southern Weddell Sea shelf. The inflow had a geostrophic velocity core of ~5 cm s^{-1} and was characterized by the highest δ^3He -rates observed in the transect (not shown). δ^3He quantifies the contribution of mantle Helium from mid-ocean ridges in a water mass such as CDW and its derivatives (Well et al., 2003; Ryan et al., 2016), thus underlining the deep-water source of the mWDW.

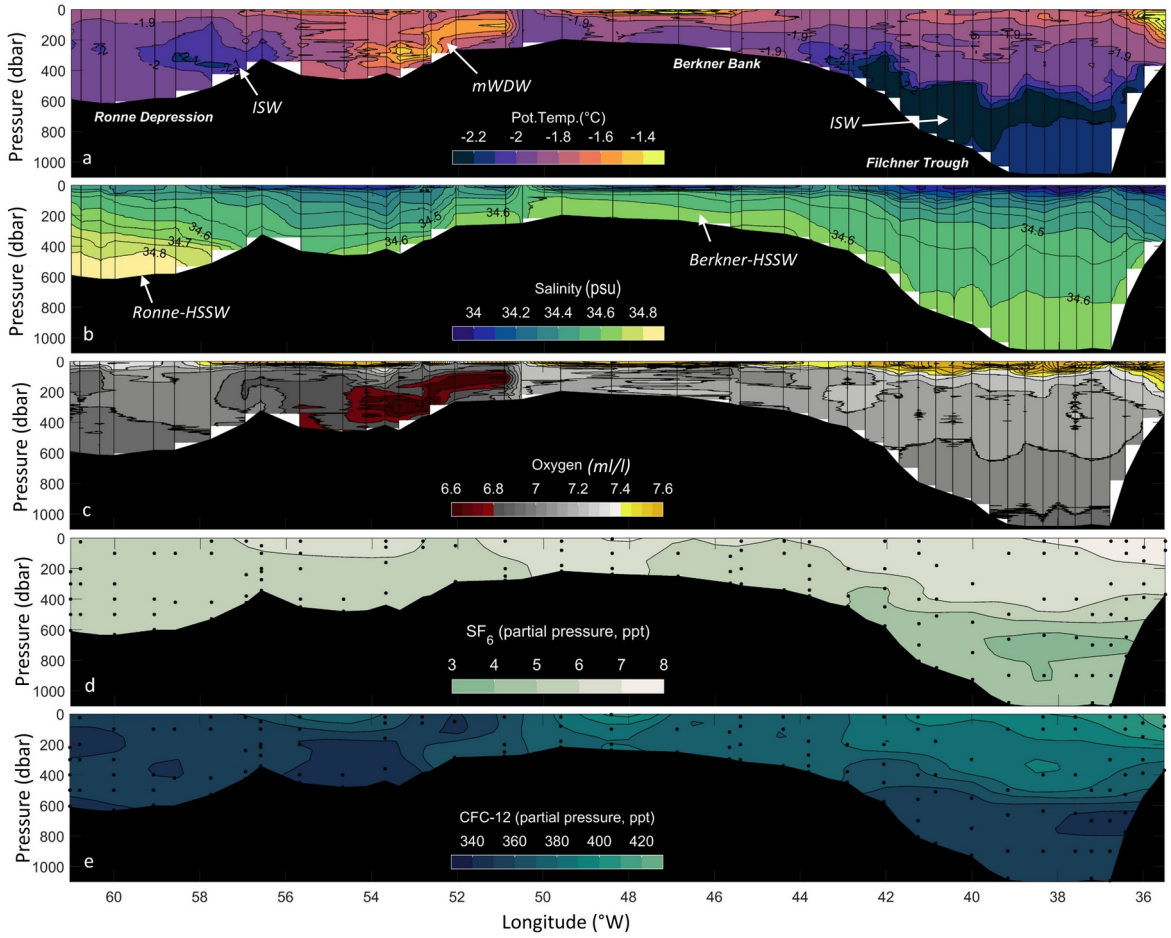

Figure 3: Properties along the FRIS front in austral summer 2018: a) potential temperature (°C), b) salinity; c) oxygen (ml/l); d) SF6 (ppt), and e) CFC-12 (ppt). Station locations can be found in Figure 1 and are indicated by vertical black lines in panels a-c and by black dots in panels d-e. Objective mapping was used to interpolate between stations in panels d and e.

Filchner Trough was strongly dominated by ISW extending across its entire width, with a minimum temperature of <-2.2°C (Figure 3a) leaning against and encroaching up the western flank between depths of 300-900 m. The ISW core contained salinities of 34.55-34.60 and agreed with a well-defined outflow core of 1-5 cm s^{-1} (Figure 5). Noble gas tracers were highly enriched in the western flank's ISW-outflow, presenting the highest ΔHe and ΔNe values (not shown) found along the FRIS front, containing as much as 1% GMBW (Figure 4a). Another outflow is seen against the eastern flank (Darelius et al., 2014a), which has been hypothesized to be associated with eastward propagation of the ISW plume parallel to the FIS front due to the step induced by the ice shelf edge and related vorticity constraints (Darelius and Sallée, 2018). However, drillhole moorings roughly 60 km south of the FIS edge show the existence of a northward flowing branch of this water mass along the eastern flank of the cavity (H2021). The upward-sloping isohalines against the eastern flank (Figure 3b) and resulting geostrophic velocities (Figure 5) suggest an inflowing undercurrent below the outflow at around 600 m, which is consistent with recirculating ISW and Berkner-HSSW in Filchner Trough (Carmack and Foster, 1975). The surface layer showed warmer (~ -1.3°C) waters extending from the eastern corner of the transect, along with lower salinities (<34.0). These waters result from summertime warming and sea ice melt, possibly fed by the coastal current that enters the area from Brunt Ice Shelf (Nicholls et al., 2009). In this region, the oxygen content was the highest (7.6 ml l^{-1}) along the FRIS front (Figure 3c), and indicates a recent interaction of these waters with the atmosphere. This is further supported by the highest CFC-12 and SF_6-values found throughout the transect (Figure 3d,e). The lowest oxygen content of 6.6 ml l^{-1} was found in the mWDW-inflow (Figure 3c, 50-55°W), which reflects the greater age of these deep and poorly-ventilated waters (Hoppema et al., 1997). HSSW-oxygen content was slightly (by ~0.1 ml l^{-1}) lower than that of ISW, which is explained by the oxygen enrichment of the ISW during ice shelf melting due to air trapped inside the ice. Since, however, the air trapped in the shelf ice was of a pre-industrial age, it did not include any anthropogenic tracers, thus explaining the low trace gas levels in the ISW (Figure 3d,e). Overall, the hydrography, along with oxygen and noble gas tracers, confirmed the previously established circulation scheme at the FRIS front (Nicholls and Østerhus, 2004). The dominant characteristics included the HSSW inflow at 59-60°W (although the density structure did not suggest such inflow at the time of survey) and the ISW outflow

348 centered at 58°W at RIS, and the more significant ISW presence with well-defined outflow cores
349 at FIS including the highest GBMW fractions of 1.0%.

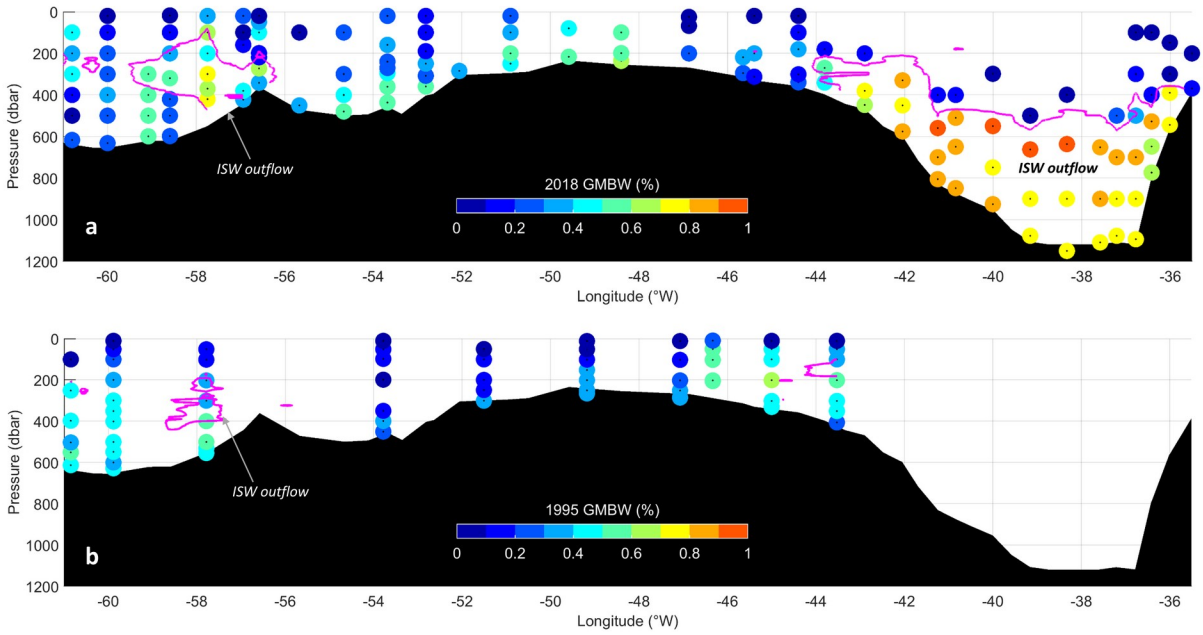

350
351 **Figure 4: Glacial basal melt water fractions (%) along FRIS shown by colored dots at the sample location and**
352 **depth in a) 2018 and b) 1995. Magenta contours in either panel marks the -2.0°C-isotherm as an indicator for**
353 **ISW outflow based on the CTD transects in these years.**

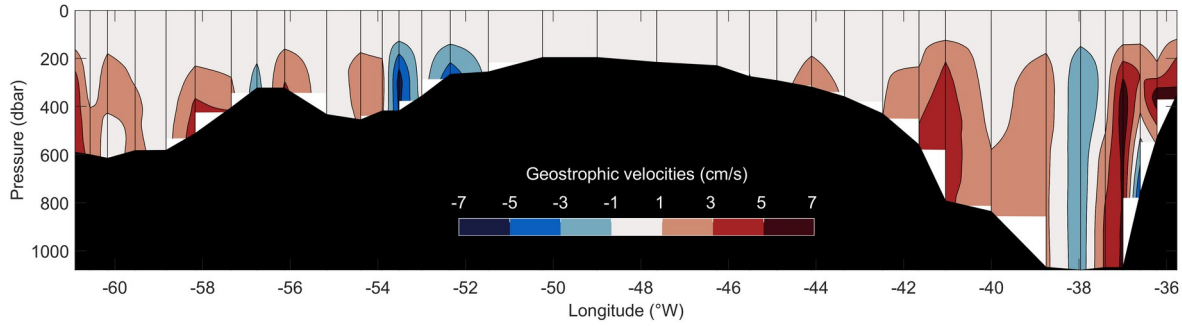

354 **Fig**
355 **ure 5: Geostrophic velocities referenced to 200 m (in cm s^{-1}) along FRIS. Positive values indicate northward**
356 **flow, i.e. into the page.**
357

358 Additonal temperature and salinity transects across the northern parts of Filchner Trough
359 and sill indicated the northward extent of the ISW upon exiting from beneath the ice shelf
360 (Figure 6). While the coldest ISW of <-2.2°C dominated at the FIS front (transect 1), the eastern
361 and western slopes of the northern Filchner Trough (transect 2 and 3) showed only traces of -
362 2.1°C-waters, indicating that the northward branch of the ISW circulation cell may be found
363 there (Figure 1). Overall, at depths below 400 m, Filchner Trough was entirely occupied by ISW

with temperatures of -2.0°C and salinities of >34.55, except for a more saline (34.60-34.65) near-bottom layer (10s of meters thick) that was just below the freezing point (Figure 7). These densest bottom waters circulate in Filchner Trough and result from a mixture of HSSW formed on Berkner Bank with the ISW outflow from underneath FIS. Most of these waters are too dense to spill northward over the ~500 m-deep sill separating Filchner Trough from the deep Weddell Sea and will thus remain confined to Filchner Trough. The overflowing waters observed north of the sill (Figure 6, transect 4) are characterized by slightly lower density of ~0.05 kg m^{-3} (Figure 7) and thus originate from the ISW layer of -2.1 to -2.0°C that occupy the 400-700 m depth layers (transect 3). The cold overflow in transect 4 was overlain by mWDW with maximum temperatures of almost 0°C and salinities of 34.5-34.6. The upward-sloping isohalines indicate enhanced northward transport at the western side of the transect, while the stations east of 31°W featured mWDW all the way to the bottom. The 2018 water mass distribution in the northern trough resembled conditions similar to those observed during earlier expeditions, as for example in 2003 (e.g. Darelius et al., 2014b). The easternmost station in transect 4 showed ISW with a lower salinity of 34.3 (Figure 7), which points to a shallower source from underneath Brunt Ice Shelf.

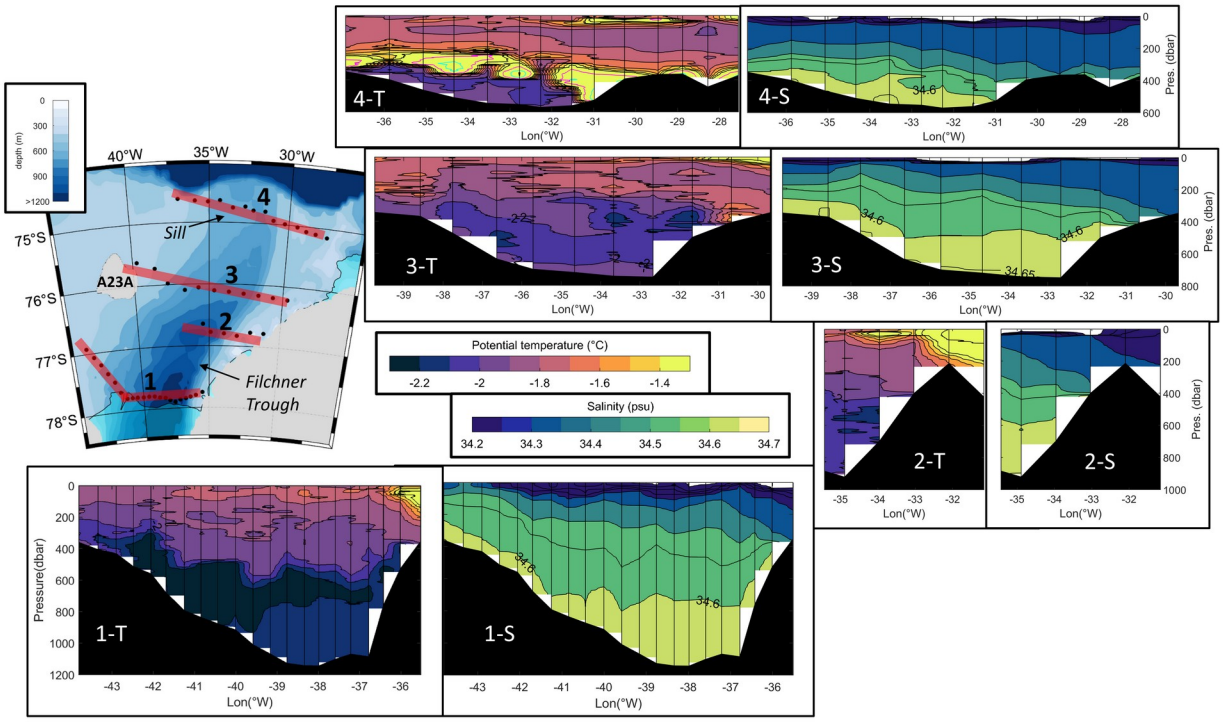

Figure 6: Filchner Trough CTD transects. The map is a zoom into the Filchner Trough region framed by the yellow box in the overview map in Figure 1 and shows the location of four transects. Stations are indicated by black dots on the map, highlighted by red lines. Bathymetry is displayed in color with 100 m-increments as

shown by the colorbar. Potential temperature (left) and salinity (right) are shown for each transect. Station locations are indicated by vertical black lines. The number on each panel refers to the numbered transects in the map. Note that the panels are scaled according to degrees longitude for a better comparison. The seafloor bathymetry was drawn based on the depth of each CTD profile, which generally was sampled down to 5-10 m above the seafloor. Separate colormaps for temperature and salinity are displayed by the colorbars in the center of the Figure. Color ranges are identical for all 4 transects. Please note that maximum temperatures in transect 4 exceed the color-limit capped at -1.3 °C. For better readability, the small cross-areas featuring -1.0°C and -0.5°C waters are displayed in magenta and green contours, respectively.

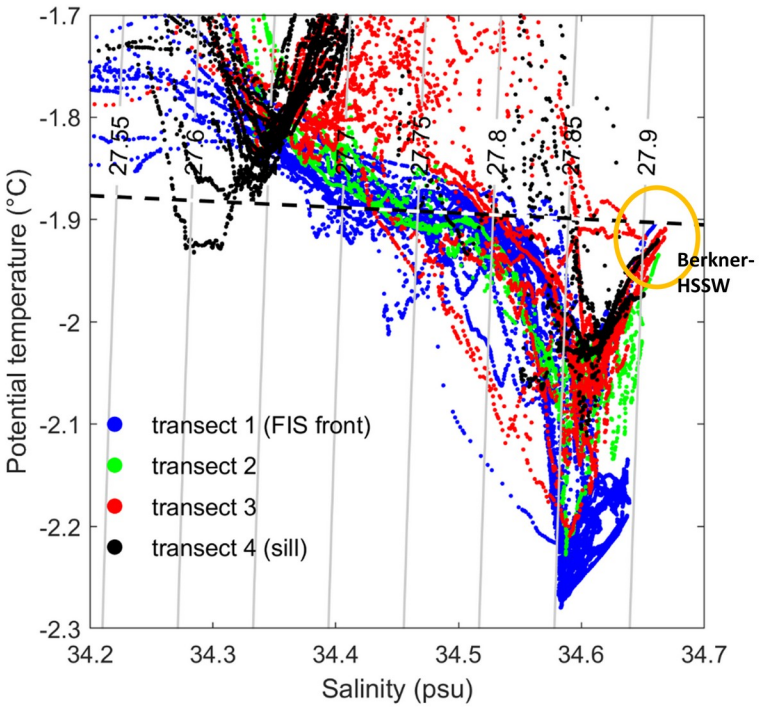

Figure 7: Temperature-salinity-diagram from CTD stations in Filchner Trough, representing water masses at and below surface freezing. Colors code the individual transects, shown in Figure 6. The yellow circle highlights the near-bottom properties related to Berkner-HSSW. σ_0–contours from 27.55 to 27.9 kg m^{-3} are marked by gray contours, the surface freezing temperature relative to salinity is shown by the black dashed line.

4) Discussion

4.1 Decadal variability in front of Ronne Ice Shelf

Sea ice conditions during early 2018 allowed us to survey the water masses of a ~750 km-long stretch along the FRIS front with unprecedented spatial resolution. Only a few expeditions have been able to access both FIS and RIS, though not with the high spatial resolution sampling

grid that was accomplished during PS111. Two such similar expeditions were carried out in austral summers of 1980 and 1995 and allow for a comparison across a four-decade time period. Similar temperature and salinity features to those shown in Figure 3 are evident in all three surveys, although the station coverage was not as spatially dense in the historic surveys. The minor thermohaline differences are therefore best displayed and compared using temperature-salinity-diagrams (Figure 8). Minimum temperatures of –2.25°C recorded in 2018 were as low as in 1980, and only marginally warmer in 1995 (Figure 8a). Salinities at the ISW temperature minimum were slightly (~0.02 psu) lower in 2018 compared with the other two periods in Filchner Trough (Figure 8c). In Ronne Depression, HSSW prominently appeared in all three surveys, with maximum salinities in 1995 and 2018 of >34.80, and slightly lower maximum salinities in 1980 of 34.78 (Figure 8b). The minimum temperature in the ISW outflow at 58°W in 2018 was -2.1°C and thus slightly lower than the other two years. This is consistent with slightly higher GBMW fractions of 0.7% in 2018 compared with 0.5% observed in 1995 inside the ISW outflow (Figure 4). The inflow of mWDW along Central Trough existed in all surveys with minor temperature differences between these years. However, the mWDW inflow is remotely controlled by slope front dynamics (Daae et al., 2017). This is further underlined by moored temperature records near the ice shelf front at 53°W, which showed considerable seasonal and interannual variability in the water mass properties (Foldvik et al., 2001), similar to the variability reported for the Filchner Trough mWDW inflow (Ryan et al., 2020). Therefore, observed differences between CTD snapshots can arise from the surveying point in time and should not be overemphasized.

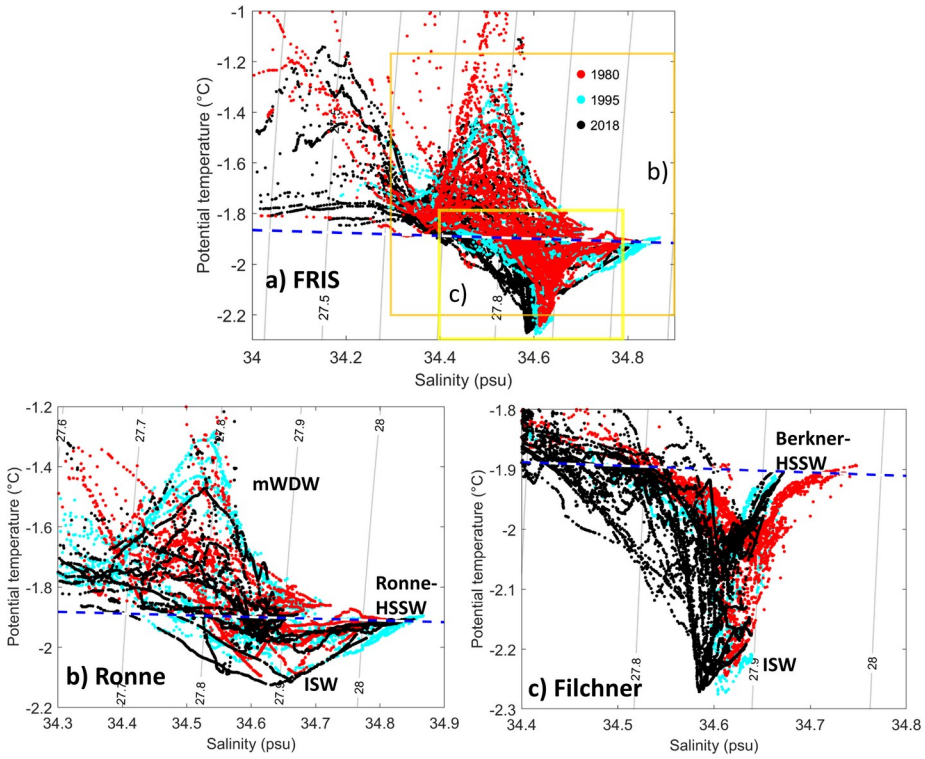

Figure 8: a) Temperature-salinity-diagram from all CTD stations along FRIS, b) from Ronne (west of 50°W), and c) Filchner (east of 43°W) CTD stations from 1980 (red), 1995 (cyan) and 2018 (black). Station locations are shown in Figure 1. σ_0–contours are shown in black lines in 0.1 kg m^{-3}-increments. The dashed line indicates the surface freezing temperature. Yellow boxes in panel a) indicate the temperature-salinity-properties of panels b) and c).

The conditions in front of RIS remained remarkably constant over time, despite the effect of the grounded icebergs after 1987 (Nøst and Østerhus, 1998; Grosfeld et al., 2001). Flow features likely stayed in the same locations due to topographic steering of the currents. One explanation for the relatively stable hydrography there may be that sharp salinity gradients developed during strong polynya events can lead to baroclinic instabilities (Chapman and Gawarkiewicz, 2003; Jenkins et al., 2004), which mix excess HSSW salt patches either into the cavity or northward. The ISW-outflow on the eastern flank of Ronne Depression is the northward extension of the sub-ice shelf circulation observed by Nicholls et al. (2004) and a comparatively small but constant feature, with most of its core at -2.0°C. The "warm" ISW temperature indicates that the HSSW-modification took place at a shallow ice shelf base (i.e. not far inside the cavity) with only a slightly lowered freezing point relative to the surface. The GMBW fractions are only slightly elevated in both 1995 and 2018 (0.5-0.7%) (Figure 4), and the tracer-based water mass dating indicates that the ISW is only 1-2 years older than its Ronne-HSSW source water (Figure

9). The ISW mixes with the adjacent waters soon after exiting RIS and is no longer observed as a distinct water mass on the southwestern Weddell Sea shelf (Nicholls et al., 2004). Earlier mooring records from the RIS front show flow parallel to the ice front, which was explained by blocking due to denser HSSW and northwestward diversion of the ISW outflow parallel to the RIS edge (Foldvik et al., 2001; Nicholls et al., 2004). Ronne Depression is the deepest part of the not-ice shelf-covered southwestern Weddell Sea shelf (Figure 1) and thus collects all dense waters formed in front of RIS. Therefore, each late summer hydrographic CTD snapshot along RIS samples the accessible remains of a reservoir with flushing time scales of roughly 10 years (Huhn et al., 2018). These long time scales explain the remarkably stable hydrography along RIS and hence provide only limited information regarding the processes taking place underneath FRIS. The anthropogenic tracer-based dating in front of RIS at 58-60°W determined the HSSW water mass age to be 4-6 years old (Figure 9), which may be partly due to older recirculating ISW on the eastern flank of Ronne Depression (Figure 3a). The old water mass age supports the concept that these winter-formed waters pool and contribute to a stable long-term reservoir without swiftly changing conditions. Apart from difficult sea ice conditions in the southwestern Weddell Sea that often inhibit ship-based access, our conclusions suggest that frequent surveys of the RIS edge region may not be needed due to the long time scales. However, since HSSW-production varies interannually and the associated volume transports into the cavity drive the circulation underneath FRIS, as will be discussed in the following, it would be desirable to obtain time series measurements of volume transports across the RIS front.

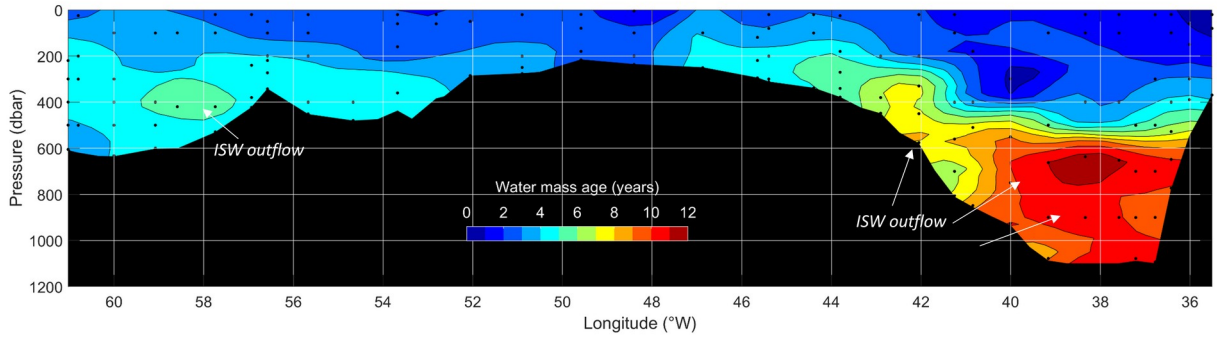

Figure 9: Water mass age based on the SF6/CFC12-ratio (see data and methods section) along the FRIS front. The bathymetry is based on station depth inferred from CTD profiles. Data are interpolated between the data points (black dots) and displayed in 1 year-color contours. ISW outflows are marked with white arrows.

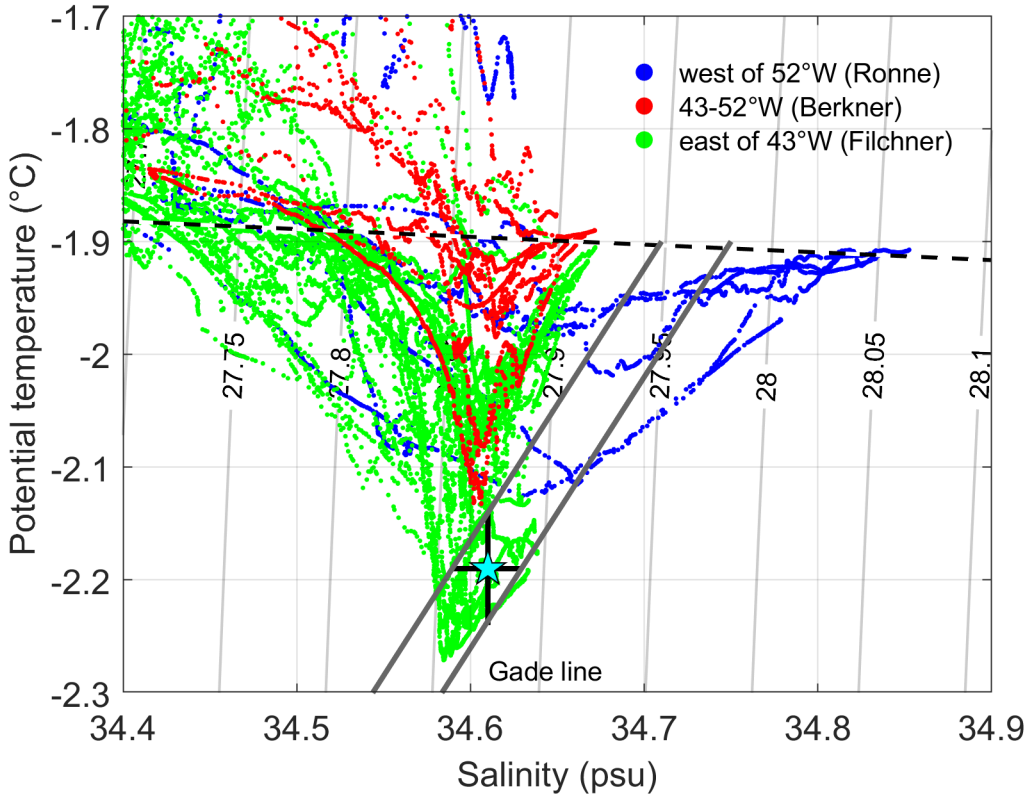

474

475 **Figure 10: Temperature-salinity-diagram from CTD stations along FRIS. Colors differentiate between Ronne**
476 **(blue), Berkner (red) and Filchner (green) stations. The blue star marks the mean temperature and salinity of**
477 **ISW colder than -2.1°C including the standard deviations indicated by the vertical and horizontal lines. The**
478 **Gade lines bound possible source water salinities (without considering mixing) at the intersection with the**
479 **line of surface freezing points (black dashed line). The Gade lines neglect the effect of heat conduction into**
480 **the ice and use a slope of 2.4 K/psu.**
481

482 4.2 On the hydrographic transition between 2017 and 2018 at the Filchner Ice Shelf front

483 The most striking feature during our 2018-survey in Filchner Trough was the large ISW-
484 covered cross-area with temperatures of <-2.2°C (Figure 3a, Figure 6 transect 1). Well-defined
485 ISW cores at similar temperatures were seen in earlier surveys, such as in 1973 (Carmack and
486 Foster, 1975), 1980 (Foldvik et al., 1985) or 2017 (Darelius and Sallée, 2018). However, these
487 ISW cores were limited to the western flank, while in 2018 the ISW below -2.2°C was found
488 across the entire width of Filchner Trough. The source of the ISW observed in the trough can be
489 inferred by applying Gade lines (Gade, 1979) in a temperature-salinity diagram. Following
490 Hutchinson et al. (2020), we applied the Gade lines based on the mean temperature and salinity
491 of the waters below -2.1°C and their standard deviations (Figure 10). The Gade line with a slope
492 of 2.4 K/psu traces the observed ISW temperatures to the surface freezing temperature and

identifies a range of resulting source salinities of 34.7-34.75. This is lower than the observed maximum Ronne-HSSW salinities of 34.84 but more saline than any other water mass sampled along FRIS. Considering that HSSW flowing underneath RIS enters a tidally-energetic environment (Makinson, 2002; Makinson and Nicholls, 1999) and mixes with local water masses of likely lower salinities, we conclude that the observed ISW in Filchner Trough could only have been sourced by Ronne-HSSW.

The 2018-conditions contrast with those observed one year earlier in 2017, when a CTD and stable isotope tracer survey found that Berkner HSSW-sourced ISW dominated in Filchner Trough (Akhoudas et al., 2020). These two different hydrographic conditions are referred to as Berkner- and Ronne-modes, and are mainly manifested by contrasting hydrographic conditions underneath the northern FIS and in Filchner Trough, as schematically illustrated in Figure 11. The two modes can also be understood as a measure of sub-FRIS circulation, forced by the production of Ronne-HSSW. When Ronne HSSW-production is weak, the local Berkner-HSSW dominates in the Filchner region, as observed in 2017 (Akhoudas et al., 2020), and is also able to enter the northern parts of FIS (Figure 11a). In contrast, an enhanced FRIS-circulation fueled by stronger inflow of Ronne-HSSW leads to enhanced ISW outflow from underneath FIS, which results in the dominance of Ronne-sourced ISW along the FIS front and in Filchner Trough, as observed in 2018 (Figure 11b).

Besides the Filchner Trough snapshot observations made in 2017 (Akhoudas et al., 2020) and 2018, a transition from Berkner- to Ronne-sourced waters was observed by drillhole moorings, which recorded CTD time series throughout this period at different locations underneath FIS (H2021, see Figure 1 in this paper for drillhole mooring locations). As illustrated in Figure 11 and shown by Figure 2 in H2021, the mooring locations deep inside the cavity only feature Ronne HSSW-sourced water masses. The northern FIS drillhole moorings, however, can be affected by circulation changes in Filchner Trough and thus were able to show the gradual transition from Berkner-sourced ISW in early 2017 to the Ronne-sourced waters in early 2018 (H2021) that we observed in Filchner Trough during PS111.

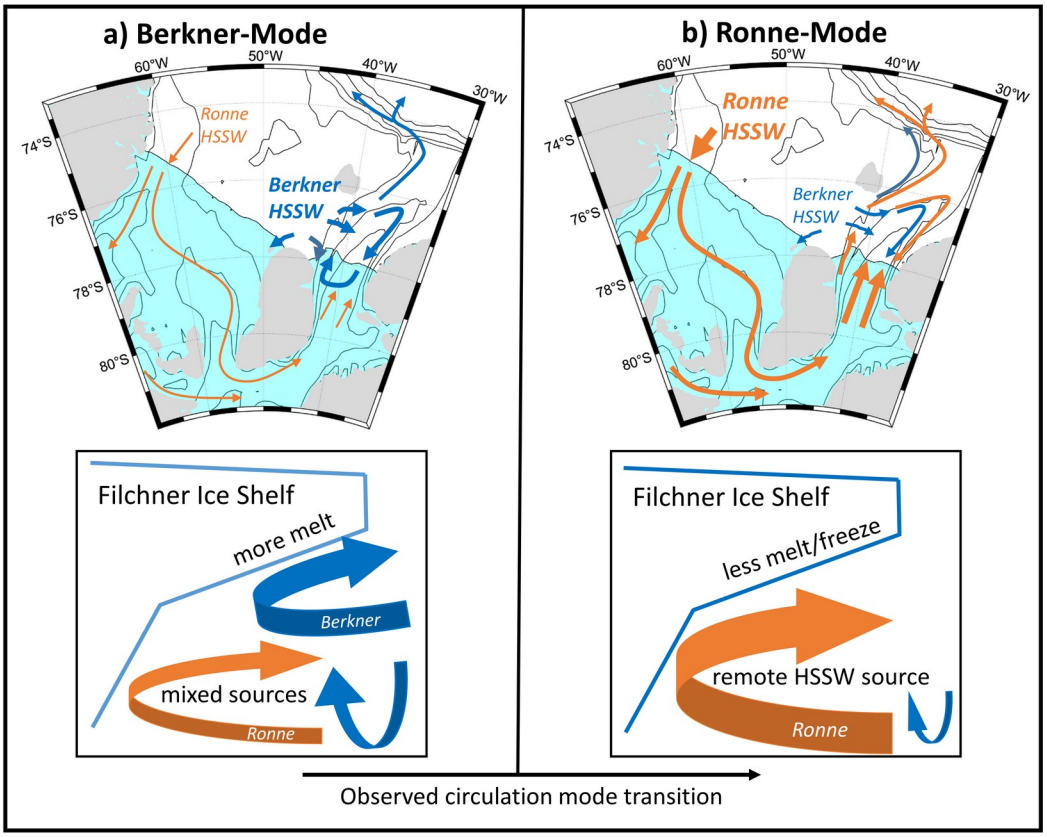

Figure 11: Schematic representation of the regional circulation and its impact on the northern FIS edge during a) Berkner- and b) Ronne-modes. The top panels indicate a map view of the circulation, while the bottom panels represent a meridional cross-section of the FIS edge. The Berkner-mode is dominated by Berkner-HSSW in Filchner Trough, associated with enhanced melt rates at the northern base of FIS. The Ronne-mode features an enhanced circulation in the cavity with an enhanced outflow of ISW from underneath FIS. Basal melting is reduced at northern FIS, but is enhanced inside the cavity. Circulation arrows are based on insights gained from the 2018 CTD survey and drillhole moorings (H2021) as well as from earlier literature-based findings.

The transition to a greater dominance of sub-FRIS waters in Filchner Trough is also reflected in GBMW fractions. Based on measurements from the same drillholes as discussed above (Figure 1), Huhn et al. (2018) report neon-based GBMW baseline fractions of 1.0-3.6% directly at the FIS base, and lower fractions of <0.4% near the bottom of the northern FIS and in Filchner Trough in 2016. These values are consistent with the (stable oxygen isotopes-based) fractions of 0.4% in Filchner Trough in 2017 reported by Akhoudas et al. (2020). In 2018, the FIS front was dominated by ISW, coincident with the highest water mass age (Figure 9) and elevated GBMW fractions of 0.8-1.0% below a depth of 600 m. These fractions directly agree with the fractions measured by Huhn et al. (2018, see their Figure 3) at the northern FIS drillhole sites. Our observations overall indicate an intensified sub-ice shelf circulation, which led to a

flushing of older water masses from the FRIS cavity into Filchner Trough, characterized by higher melt water fractions and low temperatures. This flushing was likely forced by a recent intensification of sea ice formation and HSSW-production north of RIS (Figure 12), as will be discussed in the following section.

The impact of varying circulation modes is most notable beneath the northern FIS and in Filchner Trough. Stronger inflow of HSSW via Ronne Depression leads to enhanced input of heat into the ice shelf cavity, which will be available for ice shelf melting and ISW production underneath RIS. Furthermore, stronger inflow results in intensified outflow of ISW at the FIS front, which limits melting at the northern FIS edge. Instead, freezing underneath the ice shelf increases due to a combination of ascending ISW and a rise of the local freezing temperature (Figure 11b). In contrast, in the absence of a significant northward flow out of FIS, Berkner-HSSW circulation is strong enough to impact the FIS front and locally enhance ice shelf melting (Figure 11a). This concept is supported by time series from two ApRES (autonomous phase-sensitive Radio Echo Sounders), deployed at and near a drillhole on the northeastern FIS. Basal melt rates there decreased from 1.3 m per year in 2017 to 0.8 m per year in 2018 (H2021).

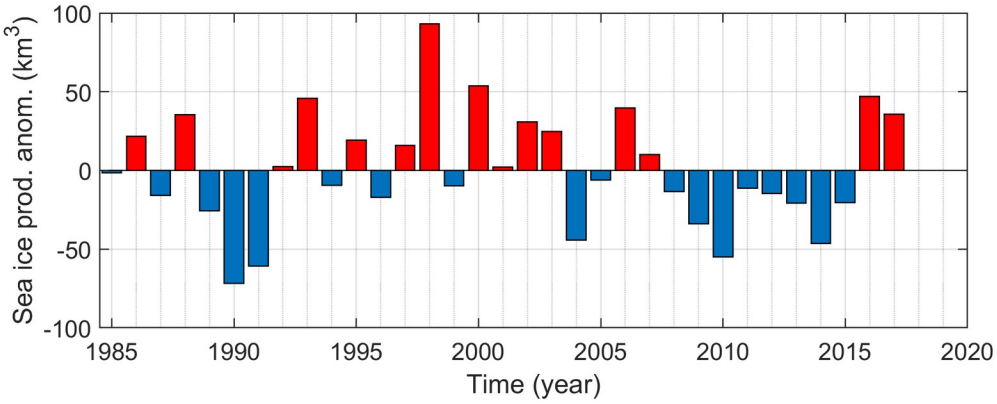

Figure 12: Sea ice production anomalies in the Ronne sector (white area in Figure 1) from 1985-2017 based on a simulation with the Finite Element Sea ice Ocean Model (FESOM; Timmermann et al., 2012) forced with data from the ERA-Interim reanalysis. The anomalies are shown relative to the mean sea ice production of 116 km^3 year^{-1}.

4.3 Decadal variability of Ronne- and Berkner-sourced Ice Shelf Water in Filchner Trough

In contrast to the low interannual variability of the hydrographic structure along RIS, the conditions off FIS are subject to greater variability impacted by local HSSW-production as well as the strength of the sub-FRIS circulation and outflow. Historical data derived from expeditions over more than four decades on the southern Weddell Sea continental shelf underline the variability and shift between Ronne- and Berkner HSSW-sourced ISW in Filchner Trough, as represented by near-bottom salinity in front of FIS (Figure 13). First, the ~0.5 psu higher initial sea surface salinities in the southwest (Figure 2b) explain the more saline Ronne-HSSW compared with Berkner-HSSW. Further, the bathymetry underneath FRIS guides Ronne-HSSW far into the cavity and toward greater pressure, which increases the basal melt potential, resulting in colder and fresher ISW. Berkner-HSSW, however, enters the shallower cavity west of Berkner Island or flows directly into Filchner Trough, and therefore interacts with the ice base at significantly shallower depths (Figure 11). This results in warmer and more saline ISW compared with Ronne HSSW-sourced ISW (see H2021). The two modes are therefore categorized by near-bottom salinities as measured in front of FIS of <34.65 (Ronne-mode, source salinity >34.7) or >34.65 (Berkner-mode, source salinity <34.7) (Figure 13). The near-bottom salinities in Filchner Trough from surveys across a 45-year time period indicate a considerable spatial and interannual variability in near-bottom water properties, suggesting that water mass characteristics alternated regularly between Ronne HSSW-derived ISW and Berkner-HSSW. However, despite relatively clear differences in the source salinities characterizing Ronne- and Berkner-modes, the densities vary only little and not consistently (not shown). For the stations considered in the source salinity computations (encircled in Figure 13), the mean potential density at depths below 600 m is 27.88 ± 0.13 kg m^{-3}, and varies less than 0.05 kg m^{-3} between the different surveys. This small range of FIS front densities, independent of the prevailing circulation mode, is still above the potential density of mWDW (~27.8 kg m^{-3}, Figure 8), which suggests that alternating modes do not directly impact the mWDW inflow dynamics. However, the bias in the available station distribution in the southern Filchner Trough limits the statistical significance of this analysis.

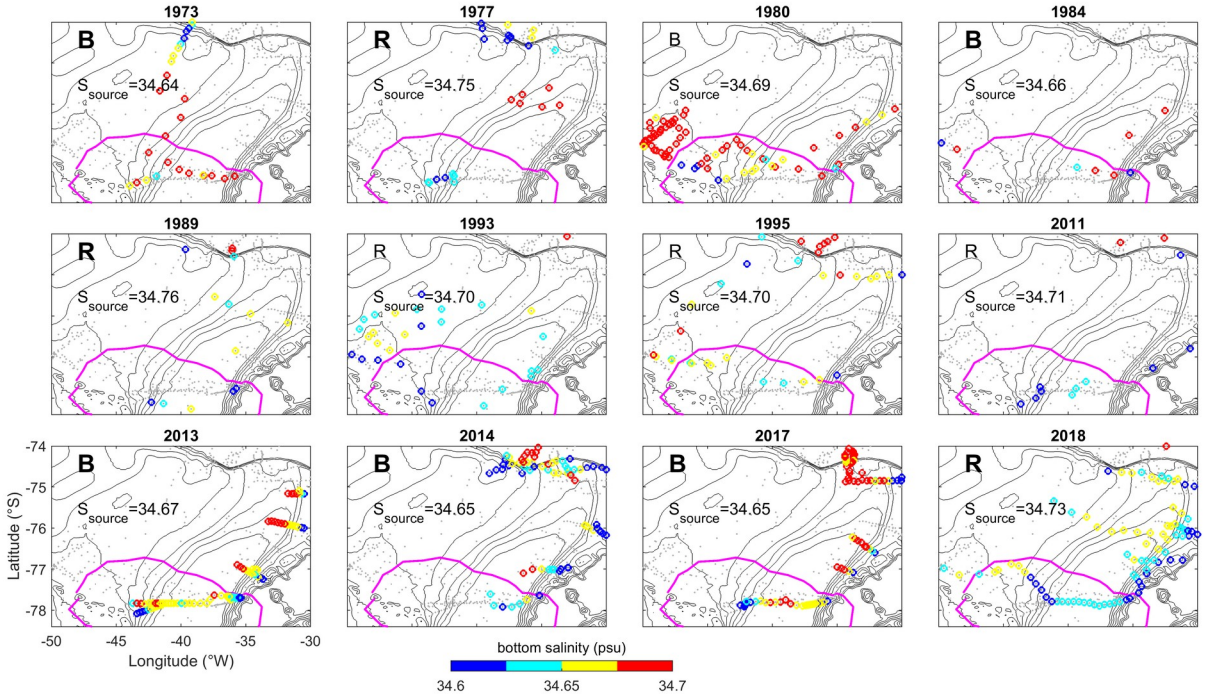

Figure 13: Maps of the Filchner region showing near-bottom salinity observed from CTD surveys since 1973. The magenta line encircles those profiles used for averaging the source water salinity of the ISW in front of Filchner Ice Shelf in order to identify the dominant circulation mode. Source salinities >34.70 and <34.70 indicate Ronne and Berkner-modes, respectively. Berkner ("B")- or Ronne("R")-mode conditions are marked by the respective letter in the upper left, the mean source salinity is provided below in each panel. A bold letter indicates that the mode is statistically significant within one standard deviation. A non-bold letter indicates statistical insignificance, i.e. too few data points or mean source salinities close to 34.70. Bathymetry (Schaffer et al., 2016) is displayed by black contours in 100 m-isobaths.

A strong Ronne-dominance as observed in 2018 leads to outflowing ISW on the western Filchner Trough slope, flushing the shelf in the Berkner-HSSW formation regions (Figure 3a and 11b). The formation of HSSW on Berkner Bank requires that surface waters reach the density of the Ronne HSSW-sourced ISW to convectively mix the water column. Once denser, the Berkner-HSSW will be able to spread and restrict the northward flow of Ronne-sourced ISW underneath FIS. Radar-sensed basal melting near the FIS front is indeed enhanced when induced by Berkner-HSSW (H2021), which produces ISW outflows that are less dense than the Ronne HSSW-sourced ISW. Hence, without enhanced sea ice formation in the Ronne polynya, driving a more vigorous cavity circulation, fresher FIS outflows would set up a feedback loop that continuously reduces the density of the Berkner-HSSW. This would promote a transition to fresher water masses in Filchner Trough with consequences for the processes at the continental shelf break. The fact that ocean densities in the lower Filchner Trough remained remarkably

616 stable under shifting source water types in the past suggests that an oscillating dominance of the
617 two circulation modes may indeed be part of the internal variability that interacts with the
618 varying forcing of the system.

619 Sea ice production and the resulting salt fluxes in the southwestern Weddell Sea are the main
620 source for Ronne-HSSW, which is the driver of the circulation underneath FRIS. Sea ice
621 production primarily depends on air-sea heat fluxes, which are further controlled by winds, sea
622 ice concentration and water column structure. In particular, extended periods of southerly and
623 southwesterly winds lead to polynya events and, consequently, large sea ice formation rates. This
624 connection between large-scale atmospheric conditions and sea ice formation in the southwestern
625 Weddell Sea is further discussed by H2021, who found that a westward displacement of the
626 Amundsen Sea Low leads to enhanced southerly winds over RIS associated with positive phases
627 of the SAM (Southern Annular Mode). For instance, a positive SAM along with vast open water
628 areas in 1998 coincided with the highest sea ice production rates within the last three decades
629 (Figure 12; Nicholls and Østerhus, 2004; Haid and Timmermann, 2013). Sea ice production in
630 the southwest Weddell Sea showed a decreasing trend after 2006 (Figure 12) coincident with a
631 decreasing number of polynya days (Paul et al., 2015), which likely resulted in the lower
632 presence of Ronne HSSW-sourced ISW in Filchner Trough before 2017. Nevertheless, sea ice
633 production increased again thereafter with two positive anomalies in 2016 and 2017 in response
634 to a period of synoptically enhanced southerly winds (H2021), which then set up the conditions
635 observed in 2018.
636

637 **5) Summary and Conclusions**

638 This paper provides a 2018-status update on the hydrographic conditions along the entire
639 length of FRIS in the southern Weddell Sea, based on a tightly-spaced CTD and noble gas tracer
640 survey. The conditions found off RIS were similar to those previously described, including a
641 strong presence of HSSW in Ronne Depression, a core of outflowing ISW and an inflow of
642 mWDW from Central Trough (Nicholls et al., 2003). Filchner Trough, however, was strongly
643 dominated by ISW (temperature <-2.0°C) along the entire ice shelf front, with a well-defined
644 core of <-2.2°C-Ronne HSSW-sourced ISW, and only slightly warmer (-2.1°C) water below
645 ~700 m (Figure 6). The outflowing ISW core leans against the western flank of Filchner Trough
646 and is identifiable in both geostrophic velocities (Figure 5) and noble gas tracers (Figure 3d-e,

Figure 4, Figure 9). Anthropogenic trace gases were used to date water masses, and the difference in water mass age between the source waters off both FIS and RIS provides insights into the circulation time scales (Figure 9). These analyses indicate a two-year travel time from Ronne Depression to the western slope of Filchner Trough at the FIS front, which agrees with earlier estimates of the direct route around Berkner Island (Nicholls and Østerhus, 2004). A less direct route through the deeper cavity must have been taken by those waters exiting via the central and eastern Filchner Trough, indicated by water masses more than 6 years older than the Ronne-HSSW source waters (Figure 9). Additional northern CTD transects (Figure 6 transects 2 and 3) show waters colder than -1.9°C in the entire Filchner Trough to the north, as well as north of the sill below 400 m (Figure 6 transect 4). These observations exemplify the export of dense FRIS-formed ISW across the sill to the Weddell Sea continental slope, widely known as a precursor for AABW and thus important for the global overturning circulation. Based on noble gas tracers, we found a maximum GBMW content of 1.0 % in the coldest ISW-core and 0.6-0.9% in the remaining ISW along the FIS front. This was close to the fractions found a few years earlier underneath FIS (Huhn et al., 2018) and not significantly different from those regions that were also measured in 1995 (Figure 4). While Filchner Trough featured Berkner-derived water mass characteristics in 2017 (Darelius and Sallée, 2018, Akhoudas et al., 2020), our 2018-survey was dominated by Ronne-sourced properties, underlining the recent shift from Berkner- to Ronne-mode (Figure 11) first identified by moorings underneath FIS in mid-2017 (H2021). This shift follows two years of strong sea ice formation in the southwestern Weddell Sea (Figure 12) and thus enhanced production of Ronne-HSSW, which fuels the circulation underneath FRIS and impacts the ice shelf-ocean interaction in two ways. First, the shift changes the spatial distribution of basal melting with lower rates near the FIS front and higher rates at greater depth inside the cavity (Figure 11). Second, dense ISW production is promoted, which is important in maintaining dense shelf waters that effectively block any larger-scale influence of mWDW. This water mass of open ocean origin is generally present at the Filchner Sill and known to penetrate southward along the eastern slope of Filchner Trough (Ryan et al., 2017).

The importance of HSSW and ISW as precursors for AABW broadens the importance of the sea ice production and processes taking place underneath FRIS, as ~50% of the deep water formed in the southern hemisphere originates from the Weddell Sea (Meredith, 2013). The southern Weddell Sea receives fresher Eastern Shelf Water via the coastal current (Nicholls et

678 al., 2009), which contributes to the observed increasing sea surface salinity from 33.5 to 34.5
679 toward the southwest (Figure 2b) and the overall higher salinity and density of the Ronne-HSSW
680 compared with HSSW formed on Berkner Bank. A strong Ronne-dominance as observed in 2018
681 leads to ISW outflow on the western Filchner Trough slope and also preconditions the ocean
682 conditions in the Berkner-HSSW formation region (Figure 3). This recycling of ISW on the
683 continental shelf suggests an internal feedback loop that would lead to a continuous freshening in
684 Filchner Trough in the absence of dense water supply from Ronne Depression under a sustained
685 Berkner-mode. Instead, the relatively stable density seen in historical data from Filchner Trough
686 suggests that the regular alternations between Ronne HSSW-derived ISW and Berkner-HSSW
687 may be part of the internal variability of the system. However, the sparse station coverage
688 between the different surveys (Figure 13) limits our understanding of the relevant processes,
689 formation mechanisms, and climatic importance of the Ronne-vs-Berkner-mode discussion.
690 Overall, the FRIS system is strongly controlled by sea ice production in the southern Weddell
691 Sea, which depends on polynyas caused by off-shore winds advecting cold air from the Antarctic
692 continent. The recent return to a Ronne-mode has been linked to anomalies in the synoptic
693 circulation over and east of the Antarctic Peninsula (H2021). If these anomalies would continue
694 to persist under climate change, a strengthening of the density barrier at the continental slope,
695 maintaining low melt rates of FRIS, could be a possible response. However, HSSW-formation
696 depends on surface forcing and on sea surface properties impacting stratification. For instance,
697 local changes in sea ice formation or glacial melt distribution, as might be expected under
698 continued warming (Timmermann and Hellmer, 2013; Hellmer et al., 2017), may negatively
699 impact the dense water production on the southern Weddell Sea continental shelf and thus
700 weaken the oceanic protection of FRIS. The global importance of the Antarctic Ice Sheet
701 underlines the need for in-situ observations such as those collected during 2018 as well as from
702 moorings on the shelf and underneath FRIS, complemented with autonomous platforms such as
703 floats and gliders. Such detailed observations are necessary to monitor potential changes around
704 FRIS and to advance the process understanding in order to improve numerical models and reduce
705 their uncertainties in projecting future sea level rise.

706 **Acknowledgments**

707 This study used samples and data provided by the Alfred Wegener Institute Helmholtz-
708 Center for Polar- and Marine Research in Bremerhaven (Grant No. AWI-PS111_00). We thank

709 Captain Schwarze and the crew of *RV Polarstern* for a very successful expedition. Andreas
710 Wisotzki carefully measured oxygen content from water samples during the expedition and
711 processed the PS111 CTD data, downloadable under:
712 https://doi.org/10.1594/PANGAEA.897280. Additional datasets used in this paper can be found
713 at: https://doi.org/10.1594/PANGAEA.860066 and https://folk.uib.no/ngfso/Data/CTD/ (historic
714 1995 and 1980 CTD data), https://doi.pangaea.de/10.1594/PANGAEA.895579 (PS111
715 thermosalinograph); https://doi.pangaea.de/10.1594/PANGAEA.913625 (PS111 meteorology);
716 https://issues.pangaea.de/browse/PDI-26756 (tracer data publication in progress). We greatly
717 appreciate the thorough comments and constructive criticism of Katherine Hutchinson and one
718 anonymous reviewer and thank the editor Laurie Padman for his efforts in handling our paper.

719 **References**

720 Akhoudas, C., Sallée, J.-B., Reverdin, G., Aloisi, G., Benetti, M., Vignes, L., Gelado, M. (2020).
721 Ice Shelf Basal Melt and Influence on Dense Water Outflow in the Southern Weddell Sea.
722 Journal of Geophysical Research: Oceans 125, e2019JC015710.
723 https://doi.org/10.1029/2019JC015710.

724 Alfred-Wegener-Institut Helmholtz-Zentrum für Polar- und Meeresforschung, 2017. Polar
725 Research and Supply Vessel POLARSTERN Operated by the Alfred-Wegener-Institute.
726 Journal of large-scale research facilities 3, A119, http://dx.doi.org/10.17815/jlsrf-3-163.

727 Beaird, N., Straneo, F., Jenkins, W. (2015). Spreading of Greenland meltwaters in the ocean
728 revealed by noble gases. Geophysical Research Letters, 42(18), 7705–7713.
729 https://doi.org/10.1002/2015GL065003.

730 Broeke, M. van den (2005). Strong surface melting preceded collapse of Antarctic Peninsula ice
731 shelf. Geophysical Research Letters 32. https://doi.org/10.1029/2005GL023247.

732 Bullister, J. L., D. P. Wisegarver, F. A. Menzia (2002). The solubility of sulfur hexafluoride in
733 water and sea water. Deep-Sea Research I, 49, 175-187.

734 Bullister, J.L. (2017). Atmospheric Histories (1765-2015) for CFC-11, CFC-12, CFC-113, CCl4,
735 SF6 and N2O (NCEI Accession 0164584). NOAA National Centers for Environmental
736 Information. Unpublished Dataset. doi: 10.3334/CDIAC/otg.CFC_ATM_Hist_2015.

737 Bulsiewicz, K., H. Rose, O. Klatt, A. Putzka, W. Roether (1998). A capillary-column
738 chromatographic system for efficient chlorofluoromethane measurement in ocean waters; J.
739 of Geoph. Res., 103, 15959-15970.

740 Carmack, E.C., Foster, T.D., 1975. Circulation and distribution of oceanographic properties near
741 the Filchner Ice Shelf. Deep Sea Research and Oceanographic Abstracts 22, 77–90.
742 https://doi.org/10.1016/0011-7471(75)90097-2

743 Chapman, D.C., Gawarkiewicz, G. (1997). Shallow Convection and Buoyancy Equilibration in
744 an Idealized Coastal Polynya. J. Phys. Oceanogr. 27, 555–566. https://doi.org/10.1175/1520-
745 0485(1997)027<0555:SCABEI>2.0.CO;2.

746 Clarke, W. B., Beg, M. A., & Craig, H. (1969). Excess 3He in the sea: Evidence for terrestrial
747 primodal helium. Earth and Planetary Science Letters, 6(3), 213–220.
748 https://doi.org/10.1016/0012-821X(69)90093-4.

749 Daae, K., Hattermann, T., Darelius, E., Fer, I. (2017). On the effect of topography and wind on
750 warm water inflow—An idealized study of the southern Weddell Sea continental shelf
751 system. Journal of Geophysical Research: Oceans 122, 2622–2641.
752 https://doi.org/10.1002/2016JC012541

753 Daae, K., Hattermann, T., Darelius, E., Mueller, R.D., Naughten, K.A., Timmermann, R.,
754 Hellmer, H.H. (2020). Necessary Conditions for Warm Inflow Toward the Filchner Ice Shelf,
755 Weddell Sea. Geophysical Research Letters 47, e2020GL089237.
756 https://doi.org/10.1029/2020GL089237

757 Darelius, E., Makinson, K., Daae, K., Fer, I., Holland, P.R., Nicholls, K.W., 2014a. Hydrography
758 and circulation in the Filchner Depression, Weddell Sea, Antarctica. Journal of Geophysical
759 Research: Oceans 119, 5797–5814. https://doi.org/10.1002/2014JC010225

760 Darelius, E., Strand, K.O., Østerhus, S., Gammeslrød, T., Årthun, M., Fer, I., 2014b. On the
761 Seasonal Signal of the Filchner Overflow, Weddell Sea, Antarctica. J. Phys. Oceanogr. 44,
762 1230–1243. https://doi.org/10.1175/JPO-D-13-0180.1

763 Darelius, E., Fer, I., Nicholls, K.W. (2016). Observed vulnerability of Filchner-Ronne Ice Shelf
764 to wind-driven inflow of warm deep water. Nat Commun 7, 12300.
765 https://doi.org/10.1038/ncomms12300.

766 Darelius, E., Sallée, J.B. (2018). Seasonal Outflow of Ice Shelf Water Across the Front of the
767 Filchner Ice Shelf, Weddell Sea, Antarctica. Geophys Res Lett 45, 3577–3585.
768 https://doi.org/10.1002/2017GL076320.

769 Dee, D. P., Uppala, S., Simmons, A., Berrisford, P., Poli, P., Kobayashi, S., Andrae, U.,
770 Balmaseda, M., Balsamo, G., Bauer, d. P., et al. (2011). The ERA-Interim reanalysis:
771 Configuration and performance of the data assimilation system, Quarterly Journal of the
772 royal meteorological society, 137, 553–597.

773 Driemel et al (2017). From pole to pole: 33 years of physical oceanography onboard R/V
774 Polarstern. Earth Syst. Sci. Data, 9, 211-220, doi:10.5194/essd-9-211-2017.

775 Foldvik, A., T. Gammelsrød, and T. Tørresen (1985a), Circulation and water masses on the
776 southern Weddell Sea shelf, in Oceanology of the Antarctic Continental Shelf, Antarct. Res.
777 Ser., vol. 43, edited by S. S. Jacobs, pp. 5– 20, AGU, Washington, D. C.
778 https://doi.org/10.1029/AR043p0005

779 Foldvik, A., Gammelsrød, T., Nygaard, E., Østerhus, S. (2001). Current measurements near
780 Ronne Ice Shelf: Implications for circulation and melting. Journal of Geophysical Research:
781 Oceans 106, 4463–4477. https://doi.org/10.1029/2000JC000217.

782 Gade, H.G., 1979. Melting of Ice in Sea Water: A Primitive Model with Application to the
783 Antarctic Ice Shelf and Icebergs. J. Phys. Oceanogr. 9, 189–198.

784 Gammelsrød, T., and N. Slotsvik (1981). Hydrographic and current measurements in the
785 southern Weddell Sea 1979/80, *Polarforschung*, *51*, 101–111.

786 Gammelsrød, T., Foldvik, A., Nøst, O.A., Foldvik, Ø., Anderson, L.G., Fogelqvist, E., Olsson,
787 K., Tanhua, T., Jones, E.P., Østerhus, S. (1994). Distribution of Water Masses on the
788 Continental Shelf in the Southern Weddell Sea, in: The Polar Oceans and Their Role in
789 Shaping the Global Environment. American Geophysical Union (AGU), pp. 159–176. https://
790 doi.org/10.1029/GM085p0159.

791 Gordon, A.L., Huber, B.A., Abrahamsen, E.P. (1993). Interannual Variability of the outflow of
792 Weddell Sea Bottom Water. Geophysical Research Letters n/a, e2020GL087014.
793 https://doi.org/10.1029/2020GL087014.

794 Grosfeld, K., Schröder, M., Fahrbach, E., Gerdes, R., Mackensen, A. (2001). How iceberg
795 calving and grounding change the circulation and hydrography in the Filchner Ice Shelf-
796 Ocean System. Journal of Geophysical Research: Oceans 106, 9039–9055.
797 https://doi.org/10.1029/2000JC000601.

798 Haid, V., Timmermann, R. (2013). Simulated heat flux and sea ice production at coastal
799 polynyas in the southwestern Weddell Sea. Journal of Geophysical Research: Oceans 118,
800 2640–2652. https://doi.org/10.1002/jgrc.20133.

801 Hattermann, T. (2018). Antarctic Thermocline Dynamics along a Narrow Shelf with Easterly
802 Winds. J. Phys. Oceanogr. 48, 2419–2443. https://doi.org/10.1175/JPO-D-18-0064.1.

803 Hattermann, T., Nicholls, K. W., Hellmer, H. H., Davis, P. E. D., Janout, M., Østerhus, S.,
804 Schlosser, E., Rohardt, G., Kanzow, T., Observed interannual changes beneath Filchner-
805 Ronne Ice Shelf linked to large-scale atmospheric circulation. Nature Communications,
806 accepted manuscript 20-20807B.

807 Hellmer, H.H., Kauker, F., Timmermann, R., Determann, J., Rae, J. (2012). Twenty-first-century
808 warming of a large Antarctic ice-shelf cavity by a redirected coastal current. Nature 485,
809 225–228. https://doi.org/10.1038/nature11064.

810 Hellmer, H.H., Kauker, F., Timmermann, R., Hattermann, T. (2017). The Fate of the Southern
811 Weddell Sea Continental Shelf in a Warming Climate. J. Climate 30, 4337–4350.
812 https://doi.org/10.1175/JCLI-D-16-0420.1.

813 Hohmann, R., Schlosser, P., Jacobs, S., Ludin, A., & Weppernig, R. (2002). Excess helium and
814 neon in the southeast Pacific: Tracers for glacial meltwater. Journal of Geophysical Research,
815 107(C11), 3198. https://doi.org/10.1029/2000JC000378.

816 Hoppema, M., E. Fahrbach and M. Schröder (1997). On the Total carbon dioxide and oxygen
817 signature of the Circumpolar Deep Water in the Weddell Gyre. *Oceanologica Acta* 20: 783-
818 798. http://archimer.ifremer.fr/doc/00093/20434/.

819 Huhn, O., Rhein, M., Rodehacke, C., Roether, W., & Schodlok, M. P. (2008). Evidence of deep-
820 and bottom-water formation in the western Weddell Sea. Deep Sea Research Part II: Topical
821 Studies in Oceanography, 55(8), 1098–1116. https://doi.org/10.1016/j.dsr2.2007.12.015.

822 Huhn, O., M. Rhein, M. Hoppema, S. van Heuven (2013). Decline of deep and bottom water
823 ventilation and slowing down of anthropogenic carbon storage in the Weddell Sea, 1984-
824 2011. Deep-Sea Research I, 76, 66-84. DOI: 10.1016/j.dsr.2013.01.005.

825 Huhn, O., Hattermann, T., Davis, P.E.D., Dunker, E., Hellmer, H.H., Nicholls, K.W., Østerhus,
826 S., Rhein, M., Schröder, M., Sültenfuß, J. (2018). Basal Melt and Freezing Rates From First
827 Noble Gas Samples Beneath an Ice Shelf. Geophysical Research Letters 45, 8455–8461.
828 https://doi.org/10.1029/2018GL079706.

829 Hutchinson, K., Deshayes, J., Sallee, J.-B., Dowdeswell, J.A., Lavergne, C. de, Ansorge, I., Luyt,
830 H., Henry, T., Fawcett, S.E., 2020. Water Mass Characteristics and Distribution Adjacent to
831 Larsen C Ice Shelf, Antarctica. Journal of Geophysical Research: Oceans 125,
832 e2019JC015855. https://doi.org/10.1029/2019JC015855.

833 Janout, Markus A; Hellmer, Hartmut H; Schröder, Michael; Wisotzki, Andreas (2019): Physical
834 oceanography during POLARSTERN cruise PS111 (ANT-XXXIII/2). Alfred Wegener
835 Institute, Helmholtz Centre for Polar and Marine Research, Bremerhaven, PANGAEA,
836 https://doi.org/10.1594/PANGAEA.897280.

837 Jenkins, A., Holland, D.M., Nicholls, K.W., Schröder, M., Østerhus, S. (2004). Seasonal
838 ventilation of the cavity beneath Filchner-Ronne Ice Shelf simulated with an isopycnic
839 coordinate ocean model. Journal of Geophysical Research: Oceans 109.
840 https://doi.org/10.1029/2001JC001086.

841 Levitus, S., Locarnini, R. A., Boyer, T. P., Mishonov, A. V., Antonov, J. I., Garcia, H. E.,
842 Baranova, O. K., Zweng, M. M., Johnson, D. R., and Seidov, D. (2010). World ocean atlas
843 2009.

844 Loose, B., & Jenkins, W. J. (2014). The five stable noble gases are sensitive unambiguous tracers
845 of glacial meltwater. Geophysical Research Letters, 41(8), 2835–2841.
846 https://doi.org/10.1002/2013GL058804.

847 Makinson, K., Nicholls, K.W. (1999). Modeling tidal currents beneath Filchner-Ronne Ice Shelf
848 and on the adjacent continental shelf: Their effect on mixing and transport. Journal of
849 Geophysical Research: Oceans 104, 13449–13465. https://doi.org/10.1029/1999JC900008.

850 Makinson, K., (2002). Modeling Tidal Current Profiles and Vertical Mixing beneath Filchner–
851 Ronne Ice Shelf, Antarctica. J. Phys. Oceanography 32, 14.

852 Meredith, M.P. (2013). Replenishing the abyss. Nature Geosci 6, 166–167.
853 https://doi.org/10.1038/ngeo1743.

854 Nicholls, K.W., Padman, L., Schröder, M., Woodgate, R. Jenkins, A., Østerhus, S. (2003). Water
855 mass modification over the continental shelf north of Ronne Ice Shelf, Antarctica. J.
856 Geophys. Res. 108, 3260. https://doi.org/10.1029/2002JC001713.

857 Nicholls, K.W., Makinson, K., Østerhus, S. (2004). Circulation and water masses beneath the
858 northern Ronne Ice Shelf, Antarctica. Journal of Geophysical Research: Oceans 109.
859 https://doi.org/10.1029/2004JC002302.

860 Nicholls, K.W., Østerhus, S. (2004). Interannual variability and ventilation timescales in the
861 ocean cavity beneath Filchner-Ronne Ice Shelf, Antarctica. Journal of Geophysical Research:
862 Oceans 109. https://doi.org/10.1029/2003JC002149.

863 Nicholls, K.W., Østerhus, S., Makinson, K., Gammelsrød, T., Fahrbach, E. (2009). Ice-ocean
864 processes over the continental shelf of the southern Weddell Sea, Antarctica: A review. Rev.
865 Geophys. 47, RG3003. https://doi.org/10.1029/2007RG000250

866 Nøst, O. A., S. Østerhus (1998), Impact of grounded icebergs on the hydrographic conditions
867 near the Filchner Ice Shelf, Antarctica, Ocean, Ice and Atmosphere: Interactions at the
868 Antarctic Continental Margin, Antarct. Res. Ser., 75S. Jacobs, R. Weiss, 269–286, *AGU,*
869 Washington, D.C.

870 Nøst, O.A., Biuw, M., Tverberg, V., Lydersen, C., Hattermann, T., Zhou, Q., Smedsrud, L.H.,
871 Kovacs, K.M. (2011). Eddy overturning of the Antarctic Slope Front controls glacial melting
872 in the Eastern Weddell Sea. Journal of Geophysical Research: Oceans 116.
873 https://doi.org/10.1029/2011JC006965.

874 Orsi, A.H., Johnson, G.C., Bullister, J.L.(1999). Circulation, mixing, and production of Antarctic
875 Bottom Water. Progress in Oceanography 43, 55–109. https://doi.org/10.1016/S0079-
876 6611(99)00004-X.

877 Paolo, F.S., Fricker, H.A., Padman, L. (2015). Volume loss from Antarctic ice shelves is
878 accelerating. Science 348, 327–331. https://doi.org/10.1126/science.aaa0940.

879 Paul, S., Willmes, S., Heinemann, G. (2015). Long-term coastal-polynya dynamics in the
880 southern Weddell Sea from MODIS thermal-infrared imagery. The Cryosphere 9, 2027–
881 2041. https://doi.org/10.5194/tc-9-2027-2015.

882 Rhein, M., R. Steinfeldt, O. Huhn, J. Sültenfuß, T. Breckenfelder (2018), Greenland submarine
883 melt water observed in the Labrador and Irminger Sea. Geophys. Res. Lett., 45, 10,570-
884 10,578, doi:10.1029/2018GL079110.

885 Rignot, E., Mouginot, J., Scheuchl, B., van den Broeke, M., van Wessem, M.J., Morlighem, M.
886 (2019). Four decades of Antarctic Ice Sheet mass balance from 1979–2017. Proc Natl Acad
887 Sci USA 116, 1095–1103. https://doi.org/10.1073/pnas.1812883116.

888 Rott, H., Skvarca, P., Nagler, T. (1996). Rapid Collapse of Northern Larsen Ice Shelf,
889 Antarctica. Science 271, 788–792. https://doi.org/10.1126/science.271.5250.788.

890 Ryan, S., Hattermann, T., Darelius, E., Schröder, M. (2017). Seasonal cycle of hydrography on
891 the eastern shelf of the Filchner Trough, Weddell Sea, Antarctica. Journal of Geophysical
892 Research: Oceans 122, 6437–6453. https://doi.org/10.1002/2017JC012916.

893 Ryan, S., Schröder, M., Huhn, O., Timmermann, R. (2016). On the warm inflow at the eastern
894 boundary of the Weddell Gyre. Deep Sea Research Part I: Oceanographic Research Papers
895 107, 70–81. https://doi.org/10.1016/j.dsr.2015.11.002.

896 Ryan, S., Hellmer, H.H., Janout, M., Darelius, E., Vignes, L., Schröder, M., (2020).
897 Exceptionally Warm and Prolonged Flow of Warm Deep Water Toward the Filchner-Ronne
898 Ice Shelf in 2017. Geophysical Research Letters 47, https://doi.org/10.1029/2020GL088119

899 Schaffer, J., Timmermann, R., Arndt, J. E., Kristensen, S. S., Mayer, C., Morlighem, M., and
900 Steinhage, D. (2016). A global, high-resolution data set of ice sheet topography, cavity
901 geometry, and ocean bathymetry.

902 Schlosser, P. (1986). Helium: A new tracer in Antarctic oceanography. Nature, 321, 233–235.

903 **Schröder, M. (2010):** Physical oceanography during POLARSTERN cruise ANT-XII/3. *Alfred
904 Wegener Institute, Helmholtz Centre for Polar and Marine Research, Bremerhaven*,
905 *PANGAEA*, https://doi.org/10.1594/PANGAEA.742581.

906 Smethie, W. M., and R. A. Fine (2001). Rates of North Atlantic deep water formation calculated
907 from chlorofluorocarbon inventories. Deep-Sea Research I, 48, 189–215.

908 Stewart, A.L., Klocker, A., Menemenlis, D. (2018). Circum-Antarctic Shoreward Heat Transport
909 Derived From an Eddy- and Tide-Resolving Simulation. Geophys. Res. Lett. 45, 834–845.
910 https://doi.org/10.1002/2017GL075677.

911 Stewart, A.L., Thompson, A.F. (2015). Eddy-mediated transport of warm Circumpolar Deep
912 Water across the Antarctic Shelf Break. Geophys. Res. Lett. 42, 432–440.
913 https://doi.org/10.1002/2014GL062281.

914 Sültenfuß, J., Roether, W., Rhein, M. (2009). The Bremen mass spectrometric facility for the
915 measurement of helium isotopes, neon, and tritium in water. Isotopes in Environmental and
916 Health Studies 45, (2), 83-95, doi: 10.1080/10256010902871929.

917 Suess, H. E., & Wänke, H. (1963). On the possibility of a helium flux through the ocean floor.
918 Progress in Oceanography, 3, 347–353. https://doi.org/10.1016/0079-6611(65)90030-3.

919 Thompson, A.F., Stewart, A.L., Spence, P., Heywood, K.J. (2018). The Antarctic Slope Current
920 in a Changing Climate. Reviews of Geophysics 56, 741–770.
921 https://doi.org/10.1029/2018RG000624.

922 Timmermann, R., Wang, Q., Hellmer, H.H. (2012). Ice-shelf basal melting in a global finite-
923 element sea-ice/ice-shelf/ocean model. Ann. Glaciol. 53, 303–314.
924 https://doi.org/10.3189/2012AoG60A156.

925 Timmermann, R., Hellmer, H.H. (2013). Southern Ocean warming and increased ice shelf basal
926 melting in the twenty-first and twenty-second centuries based on coupled ice-ocean finite-
927 element modelling. Ocean Dynamics 63, 1011–1026. https://doi.org/10.1007/s10236-013-
928 0642-0.

929 Vaughan, D.G., Marshall, G.J., Connolley, W.M., Parkinson, C., Mulvaney, R., Hodgson, D.A.,
930 King, J.C., Pudsey, C.J., Turner, J. (2003). Recent Rapid Regional Climate Warming on the
931 Antarctic Peninsula. Climatic Change 60, 243–274.
932 https://doi.org/10.1023/A:1026021217991.

933 Wang, Q., Danilov, S., Sidorenko, D., Timmermann, R., Wekerle, C., Wang, X., Jung, T., and
934 Schröter, J. (2014). The Finite Element Sea Ice-Ocean Model (FESOM) v. 1.4: formulation
935 of an ocean general circulation model, Geoscientific Model Development, 7, 663–693.

936 Warner, M. J., and R. F. Weiss (1985). Solubilities of chlorofluorocarbons 11 and 12 in water
937 and seawater. Deep-Sea Research, 32, pp. 1485-1497.

938 Waugh, D. W., T. M. Hall, T. W. N. Haine (2003). Relationships among tracer ages. Journal of
939 Geophysical Research, 108 (C5), doi:10. 1029/2002JC001325.

940 Weiss, R. F. (1971) Solubility of Helium and Neon in Water and Seawater. J. Chem. Eng. Data
941 Vol. 16, 235–241.

942 Well, R., Roether, W., & Stevens, D. P. (2003). An additional deep-water mass in Drake Passage
943 as revealed by 3He data. Deep Sea Research Part I: Oceanographic Research Papers, 50(9),
944 1079–1098. https://doi.org/10.1016/S0967-0637(03)00050-5.
945
946
947

948 **Figure captions**
949
950 Figure 1: Map of the southern Weddell Sea including CTD stations from 2018 (black), 1995
951 (blue) and 1980 (red). Magenta stars indicate drillhole moorings mentioned in the text for
952 reference (H2021). Ice Shelves are marked with cyan shading, bathymetry (Schaffer et al., 2016)
953 is shown in blue color contours. The 500 m and 1000 m-isobaths are marked with black
954 contours. Bathymetric and geographic features referred to in the text are indicated in the map.
955 The area north of RIS inside the white line marks the region used to quantify sea ice production
956 (Figure 12). The Filchner Trough framed by the yellow lines marks the inset used in Figure 6.
957 The arrows indicate the inflow branches of modified Warm Deep Water (red) and the under-
958 FRIS circulation fueled by the inflow of High Salinity Shelf Water (orange).
959
960 Figure 2: Along-track a) temperature (°C) and b) salinity measured by the ship's
961 thermosalinograph at 11 m water depth, c) air temperature (°C), d) wind speed (m s-1) and e)
962 direction (°T); f) sea level pressure (mbar) measured locally by RV Polarstern's weather system
963 displayed against the day of February. Arrows indicating travel direction and occupation dates in
964 panel a) are provided for better orientation. Cyan shading in a) and b) indicate ice sheets and ice
965 shelves. Bathymetry contours in black mark every 500 m; the 1000 m-isobath is marked by the
966 bold line.
967
968 Figure 3: Properties along the FRIS front in austral summer 2018: a) potential temperature (°C),
969 b) salinity; c) oxygen (ml/l); d) SF6 (ppt), and e) CFC-12 (ppt). Station locations can be found in
970 Figure 1 and are indicated by vertical black lines in panels a-c and by black dots in panels d-e.
971 Objective mapping was used to interpolate between stations in panels d and e.
972
973 Figure 4: Glacial basal melt water fractions (%) along FRIS shown by colored dots at the sample
974 location and depth in a) 2018 and b) 1995. Magenta contours in either panel marks the -2.0°C-
975 isotherm as an indicator for ISW outflow based on the CTD transects in these years.
976
977 Figure 5: Geostrophic velocities referenced to 200 m (in cm s-1) along FRIS. Positive values
978 indicate northward flow, i.e. into the page.
979
980 Figure 6: Filchner Trough CTD transects. The map is a zoom into the Filchner Trough region
981 framed by the yellow box in the overview map in Figure 1 and shows the location of four
982 transects. Stations are indicated by black dots on the map, highlighted by red lines. Bathymetry is
983 displayed in color with 100 m-increments as shown by the colorbar. Potential temperature (left)
984 and salinity (right) are shown for each transect. Station locations are indicated by vertical black
985 lines. The number on each panel refers to the numbered transects in the map. Note that the panels
986 are scaled according to degrees longitude for a better comparison. The seafloor bathymetry was
987 drawn based on the depth of each CTD profile, which generally was sampled down to 5-10 m
988 above the seafloor. Separate colormaps for temperature and salinity are displayed by the
989 colorbars in the center of the Figure. Color ranges are identical for all 4 transects. Please note
990 that maximum temperatures in transect 4 exceed the color-limit capped at -1.3 °C. For better
991 readability, the small cross-areas featuring -1.0°C and -0.5°C waters are displayed in magenta
992 and green contours, respectively.
993

994 Figure 7: Temperature-salinity-diagram from CTD stations in Filchner Trough, representing
995 water masses at and below surface freezing. Colors code the individual transects, shown in
996 Figure 6. The yellow circle highlights the near-bottom properties related to Berkner-HSSW. σ0–
997 contours from 27.55 to 27.9 kg m-3 are marked by gray contours, the surface freezing
998 temperature relative to salinity is shown by the black dashed line.
999
1000 Figure 8: a) Temperature-salinity-diagram from all CTD stations along FRIS, b) from Ronne
1001 (west of 50°W), and c) Filchner (east of 43°W) CTD stations from 1980 (red), 1995 (cyan) and
1002 2018 (black). Station locations are shown in Figure 1. σ0–contours are shown in black lines in
1003 0.1 kg m-3-increments. The dashed line indicates the surface freezing temperature. Yellow boxes
1004 in panel a) indicate the temperature-salinity-properties of panels b) and c).
1005
1006 Figure 9: Water mass age based on the SF6/CFC12-ratio (see data and methods section) along
1007 the FRIS front. The bathymetry is based on station depth inferred from CTD profiles. Data are
1008 interpolated between the data points (black dots) and displayed in 1 year-color contours. ISW
1009 outflows are marked with white arrows.
1010
1011 Figure 10: Temperature-salinity-diagram from CTD stations along FRIS. Colors differentiate
1012 between Ronne (blue), Berkner (red) and Filchner (green) stations. The blue star marks the mean
1013 temperature and salinity of ISW colder than -2.0°C including the standard deviations indicated
1014 by the vertical and horizontal lines. The Gade lines bound possible source water salinities
1015 (without considering mixing) at the intersection with the line of surface freezing points (black
1016 dashed line). The Gade lines neglect the effect of heat conduction into the ice and use a slope of
1017 2.4 K/psu.
1018
1019 Figure 11: Schematic representation of the regional circulation and its impact on the northern FIS
1020 edge during a) Berkner- and b) Ronne-modes. The top panels indicate a map view of the
1021 circulation, while the bottom panels represent a meridional cross-section of the FIS edge. The
1022 Berkner-mode is dominated by Berkner-HSSW in Filchner Trough, associated with enhanced
1023 melt rates at the northern base of FIS. The Ronne-mode features an enhanced circulation in the
1024 cavity with an enhanced outflow of ISW from underneath FIS. Basal melting is reduced at
1025 northern FIS, but is enhanced inside the cavity. Circulation arrows are based on insights gained
1026 from the 2018 CTD survey and drillhole moorings (H2021) as well as from earlier literature-
1027 based findings.
1028
1029 Figure 12: Sea ice production anomalies in the Ronne sector (white area in Figure 1) from 1985-
1030 2017 based on a simulation with the Finite Element Sea ice Ocean Model (FESOM;
1031 Timmermann et al., 2012) forced with data from the ERA-Interim reanalysis. The anomalies are
1032 shown relative to the mean sea ice production of 116 km3 year-1.
1033
1034 Figure 13: Maps of the Filchner region showing near-bottom salinity observed from CTD
1035 surveys since 1973. The magenta line encircles those profiles used for averaging the source
1036 water salinity of the ISW in front of Filchner Ice Shelf in order to identify the dominant
1037 circulation mode. Source salinities >34.70 and <34.70 indicate Ronne and Berkner-modes,
1038 respectively. Berkner ("B")- or Ronne("R")-mode conditions are marked by the respective letter
1039 in the upper left, the mean source salinity is provided below in each panel. A bold letter indicates

1040 that the mode is statistically significant within one standard deviation. A non-bold letter indicates
1041 statistical insignificance, i.e. too few data points or mean source salinities close to 34.70.
1042 Bathymetry (Schaffer et al., 2016) is displayed by black contours in 100 m-isobaths.